

Stratified Taylor–Couette flow: nonlinear dynamics

Juan M. Lopez^{1,†} and Francisco Marques²

¹School of Mathematical and Statistical Sciences, Arizona State University, Tempe, AZ 85287, USA

²Departament de Física, Universitat Politècnica de Catalunya, Barcelona 08034, Spain

(Received 3 June 2021; revised 2 September 2021; accepted 6 October 2021)

A series of experiments on stratified Taylor–Couette flow in short aspect ratio wide-gap annuli found an intriguing and not-well-understood dynamics: nonlinear coherent structures appearing and disappearing periodically, along with density layering reminiscent of staircase profiles. A detailed numerical study is presented of the nonlinear dynamics near onset of instability in this setting, which explains most of the characteristics found in the experiments. The simulations show that centrifugal instability of the boundary layer on the inner rotating cylinder produces jets of angular momentum forming Taylor cells that are compressed axially due to the strong stratification. These cells are not axisymmetric from the onset, but are in fact two sets of Taylor cells displaced axially that meet in localized azimuthal defect regions where the cells are patched together; the whole structure is a rotating wave with azimuthal wavenumber $m = 1$. The presence of endwalls in this short aspect ratio annulus is critical for the understanding of the dynamics. Their impact cannot be accounted for in idealized axially periodic models. Another key ingredient is the role played by the symmetries of the system. Although the axial reflection symmetry is weakly broken by centrifugal buoyancy effects, following instability there are various branches of solutions corresponding to the different ways the system's symmetries may be broken.

Key words: Taylor–Couette flow, pattern formation

1. Introduction

Interests in stratified Taylor–Couette flows have ranged from understanding the fundamentals of the dynamics in a realizable laboratory flow, its relevance as a canonical example of the interplay between rotation, stable density stratification, velocity shear and horizontal boundaries (all common ingredients of large-scale geophysical flows in oceans

† Email address for correspondence: juan.m.lopez@asu.edu

© The Author(s), 2021. Published by Cambridge University Press. This is an Open Access article, distributed under the terms of the Creative Commons Attribution licence (<https://creativecommons.org/licenses/by/4.0/>), which permits unrestricted re-use, distribution, and reproduction in any medium, provided the original work is properly cited.

and the atmosphere), to its potential in providing insight into accretion disks (Hua, Moore & Le Gentil 1997*b*; Yavneh, McWilliams & Molemaker 2001; Shalybkov & Rüdiger 2005). Unstratified Taylor–Couette flows have been extensively studied (Tagg 1994; Grossmann, Lohse & Sun 2015). In comparison, the literature on stratified Taylor–Couette flows is more limited.

The richness of the dynamics of Taylor–Couette flow in part stems from the large set of governing parameters. There are three length scales characterizing the geometry: the radii of the inner and outer cylinders, R_i and R_o , and their height H ; these provide two governing parameters, the radius ratio $\eta = R_i/R_o$ and the aspect ratio $\gamma = H/\Delta_R$, where $\Delta_R = R_o - R_i$ is the annular gap. The rotation rates of the cylinders and the top and bottom endwalls, in general, are independent. Typically, the inner cylinder rotation rate Ω is used to define a Reynolds number $Re = \Omega R_i \Delta_R / \nu$, where ν is the kinematic viscosity, and a ratio of outer-to-inner cylinder rotation rates, μ , is introduced. Most commonly, a stationary outer cylinder is considered (with $\mu = 0$), but the richness associated with $\mu \neq 0$ is extensive (Coles 1965; Andereck, Liu & Swinney 1986). The endwalls are usually either co-rotating with one of the cylinders or are both stationary. However, their differential rotation introduces a different dynamics due to the resulting global meridional circulation (Lopez, Marques & Shen 2004). Endwalls are often viewed as a nuisance and are often ignored in theoretical and numerical models, and various experimental strategies have been tried to mitigate their impacts on the dynamics (Burin *et al.* 2006; Avila 2012; Leclercq *et al.* 2016*c*). Stratification introduces additional parameters, principally the Brunt–Väisälä buoyancy frequency, N , and the diffusivity of the stratifying agent, κ . The ratio of the inner cylinder rotation rate and the buoyancy frequency is the Froude number, $Fr = \Omega/N$, and the ratio of the kinetic viscosity and the diffusivity is the Prandtl number $Pr = \nu/\kappa$ if the stratifying agent is temperature. If stratification is due to a dissolved concentration, such as salt, this ratio is called the Schmidt number, Sc (although the two names are used for either case in the literature). The nature of the stratifying agent has important implications for the boundary conditions. For salt stratification, all boundaries are of zero-flux Neumann type, whereas with temperature stratification, some are zero flux and others are fixed temperature Dirichlet type.

Early theoretical considerations of stratified Taylor–Couette flow date back to Thorpe (1966), who determined from highly idealized model equations that stratification resulted in a higher critical inner cylinder rotation rate for instability with a reduced axial wavelength. The analysis only considered flows with a stationary outer cylinder, and the idealizations included restricting the linear stability analysis to only allowing axisymmetric and axially periodic modes. Withjack & Chen (1974) conducted some of the first experiments in vertically stratified Taylor–Couette flows. Their annulus had a radius ratio $\eta = 0.2$, various cylinder rotation ratios and linear density gradients. With increasing density gradient, instability was inhibited, with onset occurring at larger inner cylinder rotation rates, and the mode of instability broke the axisymmetry of the basic state, resulting in rotating waves, with a cellular-like structure of significantly shorter axial extent than the Taylor cells typically found in unstratified experiments (see their figures 5 and 6). Their subsequent attempt to explain their experimental observations using linear stability analysis came up short due to various idealization used (Withjack & Chen 1975); in particular, their analysis was restricted to axisymmetric flow that is periodic in the axial direction. Nevertheless, the general experimental observations that the linear density gradient inhibits onset and that the axial scale of the instability cells is diminished were borne out.

In a series of experiments, linear stability analyses and nonlinear simulations, Boubnov, Gledzer & Hopfinger (1995), Boubnov *et al.* (1996), Hua, Le Gentil & Orlandi (1997*a*)

and Caton, Janiaud & Hopfinger (1999, 2000) explored in detail stratified Taylor–Couette flows over a wide range of the governing parameters, in annuli with $\eta \sim 0.8$ and $\gamma \sim 50$. They also found experimentally that linear density gradients tend to inhibit instability, that the onset of instability is generally non-axisymmetric, unsteady and with a reduced axial length scale (see figure 6 of Boubnov *et al.* 1996). They noted that pairs of vortices originate at the inner cylinder and propagate toward the outer boundary, mixing fluid between them and that a density interface forms in the central plane of each vortex pair. The vortex pairs on diametrically opposite sides of the inner cylinder are shifted vertically by one vortex size or layer height. They also noted that how these join was not clear and that the whole pattern rotates with a constant velocity less than Ω . Their modelling efforts were incapable of reproducing these experimental observations (the experimentally observed instability is oscillatory and non-axisymmetric), primarily due to the idealizations used to make the analysis tractable. They took as their basic state the unidirectional circular Couette flow with linear stratification, and only allowed for axisymmetric and axially periodic instability modes. Hua *et al.* (1997a) relaxed the axisymmetric constraint and found primary instabilities to modes with azimuthal wavenumbers $m = 1, 2$ or 3 , depending on the parameter regime. They found that these are not spirals, but instead were reminiscent of the experimentally observed structures in Boubnov *et al.* (1996). This series of studies suggested that the large Prandtl (or Schmidt) number limit is approached when $Pr \gtrsim 10$. In the more recent experiments on stratified Taylor–Couette experiments with comparable $\gamma = 43.4$ and $\eta = 0.877$, Ibanez, Swinney & Rodenborn (2016) noted that when the outer cylinder was stationary (for $Fr = 0.48$ and $Re = 169$), ‘the flow pattern is not interpenetrating spirals, but the flow is spatially periodic in the axial direction’ and ‘temporally periodic’.

Interested in further investigating the robustness of the density layers found in the experiments of Boubnov *et al.* (1995), a series of new experiments were conducted by Oglethorpe, Caulfield & Woods (2013) using annuli with smaller η and γ , larger Re and considering both discretely and linearly stratified flows. Those experiments were followed by additional experiments with more sophisticated data acquisition techniques, and focused on the linear stratified situation with $\eta \sim 0.4$ and $\gamma \sim 3$ (Leclercq *et al.* 2016b,d; Partridge *et al.* 2016); these reported the intermittent nature of the density interfaces, where the density interface is observed to periodically mix using shadowgraph visualization. Their linear stability analysis of the unidirectional stratified Couette flow failed to reconcile the axial distance between the sharp density gradients observed in the experiment, and their nonlinear simulations assuming periodicity in the axial direction in an infinitely long annulus showed that the onset of instability breaks axisymmetry, and the resulting flows structures have much in common with those reported by Hua *et al.* (1997a). Leclercq *et al.* (2016b) note that the lack of endwalls in their nonlinear simulations may be responsible for the differences between the structures simulated and those observed experimentally. The experiments of Partridge *et al.* (2016) suggest that the distance between the density layers does not depend on the gap width between the cylinders, but rather depends on the thickness of the rotating inner cylinder boundary layer. This boundary layer is established by the meridional circulation that is driven by the vortex line bending into the corners where the rotating inner cylinder meets the stationary upper and lower endwalls (Avila *et al.* 2008; Lopez 2016; Lopez & Marques 2020).

The experiments of linearly stratified Taylor–Couette flows in an annulus with $\eta = 0.417$ and $\gamma = 3$ (Leclercq *et al.* 2016b,d; Partridge *et al.* 2016) motivate our present nonlinear numerical study including the effects of endwalls. The experiments used salt as the stratifying agent, with $Sc \sim 700$. All of the experiments cited so far used water with salt as the stratifying agent. More recent stratified Taylor–Couette experiments have used thermal

stratification (Rüdiger *et al.* 2017; Meletti *et al.* 2021). There are various advantages to using one or the other stratifying agent; Gellert & Rüdiger (2009) make a compelling case for using thermal stratification. The numerical investigation of Leclercq *et al.* (2016*b*) with periodicity in the axial direction noted that ‘changing the Schmidt number by a factor of 100 leads to qualitatively similar pictures at $Sc = 7$ and $Sc = 700$ ’. Leclercq, Nguyen & Kerswell (2016*a*) also report minimal differences between $Sc = 7$ and $Sc = 700$ for the few test cases they considered. For our study, we shall consider thermal stratification with $Pr = 6$ (corresponding to water nominally at room temperature). Using thermal stratification has the advantage that the Prandtl number is small enough to avoid the stiffness in the equations associated with the large Schmidt number of salt stratification, so that numerical simulations and experiments can be conducted at the same Prandtl number. More importantly, with salt stratification the physical boundary condition at the endwalls is zero flux and this means that the linear stratified state is not an equilibrium. The experiments clearly report the erosion of the stratification at the endwalls, and that after a very long time the salt is uniform across the entire annulus even in the absence of flow advection.

In the experimental investigation of salt-stratified Taylor–Couette flow with a very small radius ratio $\eta \approx 0.066$, Flór *et al.* (2018) found the onset of instability to consist of spiral structures confined to the inner rotating cylinder, with the spiral on the bottom being triggered first. This was a very different regime to that typically studied for stratified Taylor–Couette flow. In Lopez & Marques (2020), we reproduced these results and found that endwall effects and centrifugal buoyancy were critical ingredients for understanding the observed onset of instability and the subsequent dynamics. The rotation of the inner cylinder induces radial forces: the denser fluid is centrifuged outwards, while the lighter fluid is centrifuged inwards. These forces are orthogonal to the gravitational buoyancy. The present study includes both endwall and centrifugal buoyancy effects. Most theoretical and numerical studies have considered the axial direction to be unbounded and that the basic state is invariant in the axial and azimuthal directions, and is linearly stratified (even though linear stratification in an unbounded direction parallel to the gravity vector is problematic within the Boussinesq approximation which is typically made). Also, either implicitly or explicitly, a centrifugal approximation is made whereby the angular acceleration is assumed to be negligibly small compared with gravitational acceleration (Meletti *et al.* 2021; Robins, Kersalé & Jones 2020). Shalybkov & Rüdiger (2005) discuss the possible importance of centrifugal buoyancy, particularly for strong stratification, but do not explore its consequences as ‘the situation becomes much more complicated’. The ‘complication’ is at least partially due to the fact that even if the infinite axial extent idealization is made, with centrifugal buoyancy included the system of equations are no longer axially invariant, the basic state is no longer unidirectional and the usual stability analysis is no longer valid. Centrifugal buoyancy breaks the up–down reflection symmetry, the induced flow being more intense near the colder bottom endwall. Without considering endwalls it is not possible to understand the initial development of the instability, that propagates from the endwalls to the interior of the cylinders.

The paper is organized as follows. Section 2 describes the governing equations, the non-dimensional governing parameters, the boundary conditions and how the system is solved numerically. The symmetry of the problem is described, as is how centrifugal buoyancy weakly breaks the up–down reflection symmetry. Section 3 describes the steady axisymmetric basic state in the finite annulus, and contrasts its features with the often used unidirectional circular Couette flow with linear stratification. Section 4 considers the instability and nonlinear dynamics confined to the axisymmetric subspace, while § 5 removes the axisymmetric constraint and shows that instability sets in at lower Re

as rotating waves with azimuthal wavenumber $m = 1$ whose precession frequency is approximately one third the inner cylinder rotation rate. At higher Re , a very low frequency modulation sets in, but the main features of the flow remain those of the rotating waves. The weakly broken up–down reflection symmetry, induced by the centrifugal buoyancy, is found to play an important role in understanding the spatio-temporal structure of the flows. Section 6 discusses how the present results fit in with previous studies of stratified Taylor–Couette flows in a variety of different parameter regimes.

2. Governing equations

Consider a completely fluid-filled annulus of height H , inner radius R_i and outer radius R_o . The outer cylinder, top and bottom walls are stationary and the inner cylinder rotates at constant angular velocity Ω . The top and bottom endwalls are maintained at fixed temperatures, $T_0^* + \Delta T^*/2$ for the top endwall and $T_0^* - \Delta T^*/2$ for the bottom endwall, while both cylinders are insulated. Here, T_0^* is a reference temperature, and the temperature difference, ΔT^* , between the top and bottom endwalls is positive, so that the vertical temperature gradient is stabilizing. Gravity g points downwards. The kinematic viscosity of the Newtonian fluid is ν , its thermal diffusivity is κ and its coefficient of volume expansion is α .

Using the annular gap, $\Delta R = R_o - R_i$, as the length scale, the viscous diffusion time across the gap, $\Delta R^2/\nu$, as the time scale, ΔT^* as the temperature scale and employing the Boussinesq approximation accounting for centrifugal buoyancy (Lopez, Marques & Avila 2013), the non-dimensional governing equations are

$$\partial_t \mathbf{u} + (\mathbf{u} \cdot \nabla) \mathbf{u} = -\nabla p + \nabla^2 \mathbf{u} + Gr T \hat{\mathbf{z}} + \epsilon T (\mathbf{u} \cdot \nabla) \mathbf{u}, \quad \nabla \cdot \mathbf{u} = 0, \quad (2.1)$$

$$\partial_t T + (\mathbf{u} \cdot \nabla) T = Pr^{-1} \nabla^2 T, \quad (2.2)$$

where $\mathbf{u} = (u, v, w)$ is the non-dimensional velocity field in the cylindrical polar coordinate system (r, θ, z) , p is the dynamic pressure and $\hat{\mathbf{z}}$ is the unit vector in the vertical direction z . The term $\epsilon T (\mathbf{u} \cdot \nabla) \mathbf{u}$ accounts for centrifugal buoyancy effects. The fluid domain is $r \in [r_i, r_o] = [\eta/(1 - \eta), 1/(1 - \eta)]$, $\theta \in [0, 2\pi)$ and $z \in [-\gamma/2, \gamma/2]$, where $\eta = R_i/R_o$ is the radius ratio and $\gamma = H/\Delta R$ is the aspect ratio. We shall fix the annular geometry to $\eta = 0.417$ and $\gamma = 3$, motivated by recent experiments using these values (Leclercq *et al.* 2016*b,d*; Partridge *et al.* 2016) as well as other experiments with similar values (Woods *et al.* 2010; Oglethorpe *et al.* 2013).

The boundary conditions for temperature and velocity are

$$r = r_i : \quad \partial_r T = 0, \quad u = w = 0, \quad v = Re, \quad (2.3a)$$

$$r = r_o : \quad \partial_r T = 0, \quad u = w = v = 0, \quad (2.3b)$$

$$z = -\gamma/2 : \quad T = -1/2, \quad u = w = 0, \quad v = Re q(r), \quad (2.3c)$$

$$z = \gamma/2 : \quad T = 1/2, \quad u = w = 0, \quad v = Re q(r), \quad (2.3d)$$

where the azimuthal velocity at the corners where the rotating inner cylinder meets the stationary top and bottom endwalls has been regularized by using

$$q(r) = \exp[-c(r - r_i)], \quad \text{with } c = 100. \quad (2.4)$$

The radial function $q(r)$ is almost zero everywhere except in a narrow interval (controlled by c) close to the rotating inner cylinder. In this way the boundary condition on v is continuous, avoiding Gibbs phenomena associated with discontinuities in the numerical

simulations, and mimics the gap that exists in any real device with the inner cylinder rotating and stationary endwalls. The value of c is chosen such that q decreases from 1 to 0.05 over 3 % of the annular gap.

The non-dimensional groups appearing in the governing equations and boundary conditions are

$$\text{Prandtl number } Pr = \nu/\kappa, \tag{2.5a}$$

$$\text{Reynolds number } Re = \Omega R_i \Delta_R / \nu, \tag{2.5b}$$

$$\text{Grashof number } Gr = \alpha g \Delta T^* \Delta_R^3 / \nu^2, \tag{2.5c}$$

$$\text{relative density variation } \epsilon = \alpha \Delta T^*, \tag{2.5d}$$

$$\text{radius ratio } \eta = R_i / R_o, \tag{2.5e}$$

$$\text{aspect ratio } \gamma = H / \Delta_R. \tag{2.5f}$$

The Prandtl number is a ratio of fluid properties and is constant in a given experiment modelled by the Boussinesq approximation, where small variations in κ and ν due to temperature variations are neglected. We shall fix the Prandtl number $Pr = 6$, nominally corresponding to water at approximately 25 °C.

The Grashof number Gr and the relative density variation ϵ are proportional to the imposed temperature gradient, and their ratio is the Archimedes number

$$Ar = Gr/\epsilon = g \Delta_R^3 / \nu^2. \tag{2.6}$$

For a given experimental setting g and Δ_R are fixed, and hence Ar is essentially constant (but for small temperature variations in ν which are typically neglected under the Boussinesq approximation). So, $\epsilon = Gr/Ar$ is slaved to Gr , and so there are only two independent dynamical parameters in the problem, Re and Gr . Other non-dimensional numbers used in this and related studies are the ratio of buoyancy and rotation time scales, known as the Froude number $Fr = \Omega/N$, where $N = \sqrt{\alpha g \Delta T^* / H}$ is the Brunt–Väisälä buoyancy frequency, and $R_N = N \Delta_R^2 / \nu$, the non-dimensional buoyancy frequency, which is the ratio of the viscous and buoyancy time scales. These are related to Re and Gr

$$Fr = \frac{Re}{R_N} \frac{\Delta_R}{R_i} = \frac{Re}{R_N} \frac{(1 - \eta)}{\eta}, \quad R_N = \sqrt{\frac{Gr}{\gamma}}. \tag{2.7a,b}$$

In some studies, the bulk Richardson number, $Ri = N^2 / \Omega^2 = 1 / Fr^2$, is used.

With the non-dimensionalization we have used, Re and Gr are the non-dimensional groups that naturally appear in the governing equations and boundary conditions. We shall also fix their ratio such that $Fr = 0.53$. This is motivated by several reasons; this is the value of Fr used in our very wide-gap study (Lopez & Marques 2020) that reproduced the experimental observations of Flór *et al.* (2018). The experiments of Le Bars & Le Gal (2007), Leclercq *et al.* (2016*b,d*) and Partridge *et al.* (2016) also feature comparable values of Fr , as do the nonlinear simulations of Gellert & Rüdiger (2009).

Neglecting centrifugal buoyancy corresponds to taking the limit $\epsilon \rightarrow 0$ in (2.1). The Archimedes number corresponding to experiments with water at approximately room temperature in annuli with a gap width of approximately 10 cm is large, $Ar = 10^{10}$, and so ϵ is small, of order 10^{-2} for $Gr \sim 10^8$. Fixing $Fr = 0.53$, $Ar = 10^{10}$, $\eta = 0.417$ and $\gamma = 3$ means that, in our study with varying Re , we have $Gr = 20.8754 Re^2$ and $\epsilon = 2.08754 \times 10^{-9} Re^2$. The results all have these fixed parameter values, and only Re is varied.

The governing equations are solved using a second-order time-splitting method with consistent boundary conditions for the pressure, as in Lopez & Marques (2014, 2020). Spatial discretization is via a Galerkin–Fourier expansion in θ and Chebyshev collocation in r and z . The spatial and temporal resolution used was $n_r \times n_z \times n_\theta = 100 \times 300 \times 64$ and $\delta t = 10^{-7}$ for $Re \sim 10^3$.

The kinetic energies of the azimuthal Fourier modes of the velocity field,

$$E_m = \frac{1}{2} \int_{-\gamma/2}^{\gamma/2} \int_{r_i}^{r_o} \mathbf{u}_m \cdot \mathbf{u}_m^* r \, dr \, dz, \tag{2.8}$$

where \mathbf{u}_m is the m th Fourier mode of the velocity field and \mathbf{u}_m^* is its complex conjugate, provide a convenient way to characterize the non-axisymmetric states.

The domain and boundary conditions have a symmetry group generated by arbitrary rotations \mathcal{R}_β around the annulus axis, and a reflection \mathcal{K} about the mid-height plane. Their actions on the velocity and temperature are

$$\mathcal{R}_\beta : [u, v, w, T](r, \theta, z, t) \mapsto [u, v, w, T](r, \theta - \beta, z, t), \tag{2.9a}$$

$$\mathcal{K} : [u, v, w, T](r, \theta, z, t) \mapsto [u, v, -w, -T](r, \theta, -z, t), \tag{2.9b}$$

where β is an arbitrary angle. The rotations \mathcal{R}_β generate the group $SO(2)$, and the reflection \mathcal{K} generates the group Z_2 since \mathcal{K}^2 is the identity; \mathcal{R}_β and \mathcal{K} commute ($\mathcal{K} \mathcal{R}_\beta = \mathcal{R}_\beta \mathcal{K}$), and together they generate the group $\mathcal{G} = SO(2) \times Z_2$.

The temperature and incompressibility equations (2.2) are equivariant with respect to \mathcal{G} . However, in the Navier–Stokes equations (2.1), the last term is not equivariant; it changes sign when reflected (applying \mathcal{K}). This centrifugal buoyancy term means that the full system is not reflection symmetric. The denser fluid at the bottom endwall is centrifuged outwards, while the lighter fluid near the top endwall is centrifuged inwards, generating a large-scale circulation that breaks \mathcal{K} . In summary, if $\epsilon = 0$ then \mathcal{G} is the symmetry group of the problem, but when $\epsilon \neq 0$ the symmetry group is only $SO(2)$. With the fixed parameters being used, the symmetry-breaking effects of non-zero ϵ are negligible for small Re ; nevertheless, we maintain $\epsilon \neq 0$ as the symmetry breaking may be dynamically important for $Re \gtrsim \mathcal{O}(10^3)$.

3. Steady axisymmetric basic state

We begin by considering the steady axisymmetric basic state, denoted S_0 . It is convenient to consider it in terms of the streamfunction, ψ , azimuthal component of vorticity, ω_θ , and angular momentum, $\Gamma = rv$. In terms of these quantities, the velocity and vorticity fields are

$$\mathbf{u} = (u, v, w) = r^{-1}(-\partial_z \psi, \Gamma, \partial_r \psi), \tag{3.1}$$

$$\nabla \times \mathbf{u} = (\omega_r, \omega_\theta, \omega_z) = r^{-1}(-\partial_z \Gamma, r[\partial_z u - \partial_r w], \partial_r \Gamma). \tag{3.2}$$

Contours of ψ and Γ in a meridional (r, z) -plane give cross-sections of streamsurfaces (streamlines) and vortex surfaces (vortex lines). The governing equations, (2.1) and (2.2), restricted to the axisymmetric subspace ($\partial_\theta = 0$), are then

$$\partial_t \Gamma + [1 - \epsilon T](u \partial_r \Gamma + w \partial_z \Gamma) = (\partial_r^2 - r^{-1} \partial_r + \partial_z^2) \Gamma, \tag{3.3}$$

$$\partial_t T + (u\partial_r + w\partial_z)T = Pr^{-1}(\partial_r^2 - r^{-1}\partial_r + \partial_z^2)T, \tag{3.4}$$

$$\begin{aligned} \partial_r \omega_\theta + [1 - \epsilon T](u\partial_r \omega_\theta - r^{-1}u\omega_\theta + w\partial_z \omega_\theta - r^{-3}\partial_z \Gamma^2) \\ - \epsilon(u\partial_r u + w\partial_z u - r^{-3}\Gamma)\partial_z T + \epsilon(u\partial_r w + w\partial_z w)\partial_r T \\ = -Gr\partial_r T + (\partial_r^2 + r^{-1}\partial_r - r^{-2} + \partial_z^2)\omega_\theta. \end{aligned} \tag{3.5}$$

In the idealized situation of an infinitely long annulus without endwalls and ignoring centrifugal buoyancy by taking $\epsilon = 0$, the unidirectional linearly stratified circular Couette flow with $\Gamma = \eta Re(r_o^2 - r^2)/(1 + \eta)$, $\omega_\theta = 0$, $\psi = 0$ and $T = z/\gamma$ is an equilibrium solution of (3.3)–(3.5). If $\epsilon \neq 0$, the unidirectional flow is not an equilibrium due to the term $\epsilon r^{-3}\Gamma\partial_z T$ in (3.5), which is a source term for the azimuthal vorticity. It becomes negligible if $\epsilon \rightarrow 0$ i.e. negligible centrifugal buoyancy. Furthermore, once endwalls are considered, even if they are infinitely far apart and one ignores centrifugal buoyancy, the unidirectional flow is not a solution. For the situation currently under consideration, with the inner cylinder rotating and the outer cylinder and endwalls stationary, the vortex lines are tangential to the stationary endwalls; they all enter and leave the annulus at the corners where the rotating inner cylinder meets the endwalls. The bending of the vortex lines into these corners results in a meridional flow via the $-r^{-3}\partial_z \Gamma^2 = -2r^{-1}v\partial_z v$ term in (3.5) (Lopez 1998), setting up the endwall boundary layers (often called Ekman layers) with flow nearest the endwalls directed radially in towards the inner cylinder. This meridional flow advects the isotherms leading to horizontal temperature gradients near the corners and further contributes to the meridional flow via the $\partial_r T$ baroclinic torque term in (3.5).

Figure 1 illustrates the role of the endwalls in driving the meridional flow. The plots in the figure are oriented such that the rotating inner cylinder is the left boundary and gravity points downwards. The vortex lines are plotted with levels $\Gamma \in [0, r_i Re]$; they appear to be invariant with Re . Instead of isotherms, we have plotted contours of the axial temperature gradient $\partial_z T$, which is a constant $\partial_z T = 1/\gamma$ for $Re = 0$, and it clearly highlights the deviations from the initially imposed linear temperature stratification for $Re \neq 0$. These deviations appear near the corners where the rotating inner cylinder meets the endwalls. For very small $Re \sim 1$, $\partial_z T$ remains essentially constant and the meridional flow is solely driven by vortex line bending. When the meridional flow is sufficiently strong it is able to modify the temperature stratification, resulting in its baroclinic interaction with the meridional flow. The (r, z) -dependence of $\partial_z T$ becomes evident for $Re \gtrsim 100$, as the meridional flow is focused at the corners. Whereas the azimuthal flow scales as $v \sim Re$, the meridional flow scales as $(u, w) \sim Re^{3/2}$, and for $Re \gtrsim 10$ the meridional flow clearly forms endwall boundary layers whose thickness scales with $Re^{-1/2}$, as illustrated by the streamlines. These layers are of Bödewadt type, as in isothermal Taylor–Couette flows with stationary endwalls (Avila *et al.* 2008).

Often, the basic state is taken to be a unidirectional azimuthal z -independent flow whose r dependence corresponds to the scaled azimuthal velocity of the circular Couette flow between two infinitely long cylinders, together with a linear (in z) temperature (density) profile. When the inner cylinder rotates at non-dimensional rate Re and the outer cylinder is stationary, the circular Couette flow profile is (Taylor 1923)

$$\frac{v(r)}{Re} = \frac{\eta}{1 - \eta^2} \left(\frac{r_o}{r} - \frac{r}{r_o} \right). \tag{3.6}$$

Figure 2 compares the radial profiles of the scaled azimuthal velocity v/Re at mid-height $z = 0$ of the steady axisymmetric state S_0 for $\gamma = 3$ and $Fr = 0.53$ (for $Re < 500$, this scaled profile at $z = 0$ is independent of Re), and of the scaled circular Couette flow

Stratified Taylor–Couette flow: nonlinear dynamics

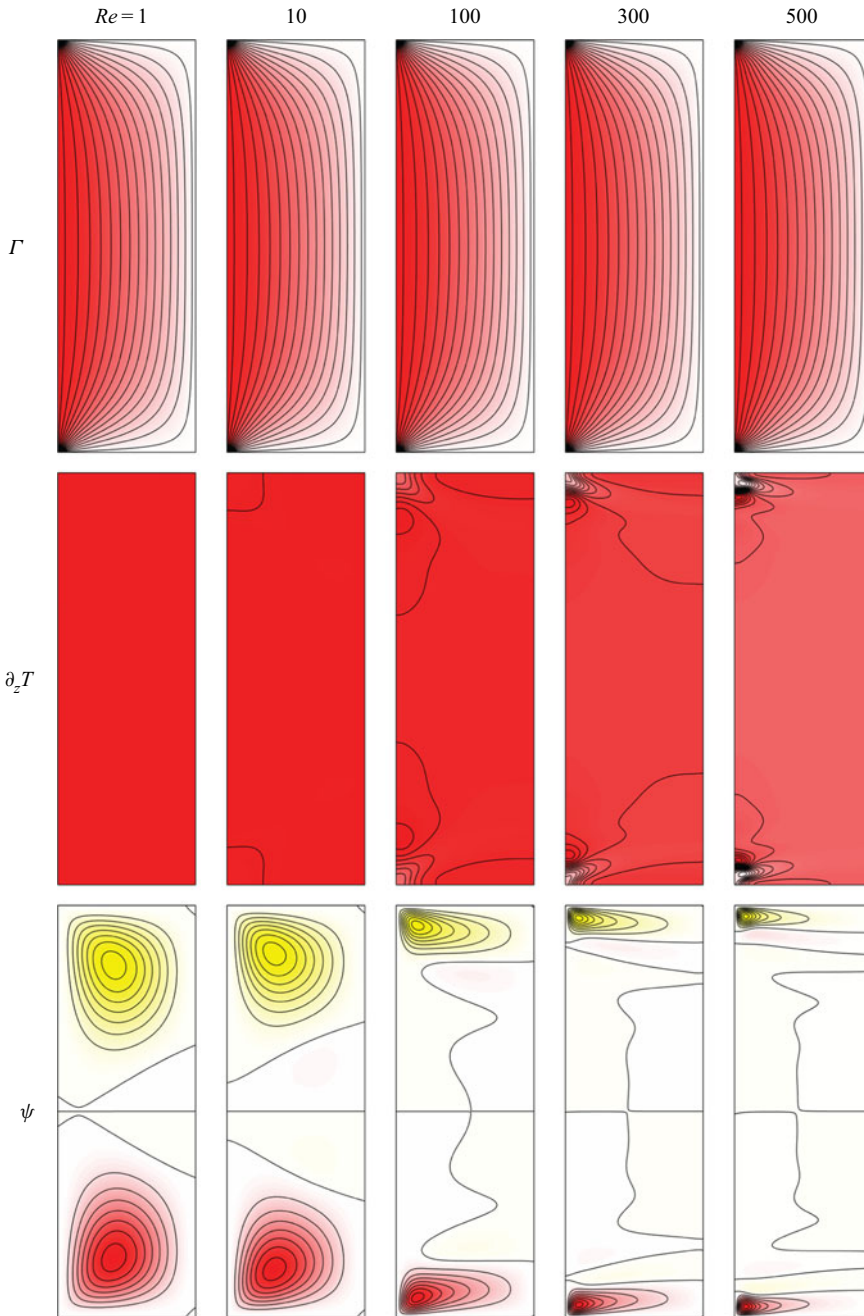


Figure 1. Contours of Γ , $\partial_z T$ and ψ of the steady axisymmetric basic state S_0 at Re as indicated. The contour levels (red positive and yellow negative) are $\Gamma \in [0, r_i Re]$, $\partial_z T \in [0, 0.33 + 4 \times 10^{-4} Re a]$ and $\psi \in [-a, a]$, where $a = 0.005 + 1.3 \times 10^{-5} Re^{3/2}$. Contours are in a meridional plane, $(r, z) \in [r_i, r_o] \times [-\gamma/2, \gamma/2]$.

(which is independent of Re), both with radius ratio $\eta = 0.417$. For the given geometry (η and γ), the two $v(r)$ profiles are very different. For example, the azimuthal velocities at mid-gap differ by approximately 30%. This is a well-known consequence of endwall

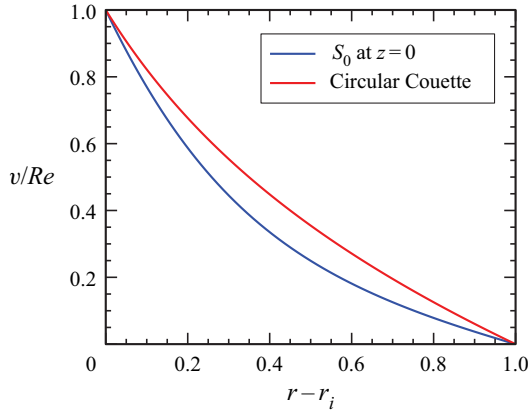


Figure 2. Radial profiles of the scaled azimuthal velocity v/Re at mid-height $z = 0$ of the steady axisymmetric state S_0 for $Re \leq 500$, $\gamma = 3$ and $Fr = 0.53$, and of the scaled azimuthal velocity of the unidirectional circular Couette flow, both for radius ratio $\eta = 0.417$.

effects (Coles & van Atta 1966). For much larger aspect ratios, $\gamma \sim \mathcal{O}(10\text{--}100)$, it is generally expected that the two radial profiles of v are in better agreement, allowing the use of the unidirectional stratified circular Couette flow in linear stability analysis (Boubnov *et al.* 1995, 1996; Caton *et al.* 2000; Molemaker, McWilliams & Yavneh 2001; Yavneh *et al.* 2001; Shalybkov & Rüdiger 2005; Park & Billant 2013; Leclercq *et al.* 2016a; Robins *et al.* 2020). However, for short aspect ratios like that studied here, endwall effects drive meridional flows and, as with unstratified Taylor–Couette flows in short aspect ratios, the resulting instabilities can differ significantly (Benjamin & Mullin 1981; Cliffe, Kobine & Mullin 1992; Lopez & Marques 2003; Abshagen *et al.* 2005a,b; Lopez & Marques 2005; Marques & Lopez 2006; Abshagen *et al.* 2008; Lopez 2016).

From figure 1, it is apparent that the steady axisymmetric basic state S_0 is essentially \mathcal{K} symmetric, even though the terms in the governing equations with ϵ as a factor break the symmetry. As noted earlier, with the choice of fixed parameters under consideration, $\epsilon \propto Re^2$ with a very small constant of proportionality. As a quantitative measure of the \mathcal{K} symmetry breaking in the flow, we introduce the symmetry measure

$$S_{\mathcal{K}} = \|\mathbf{u} - \mathcal{K}\mathbf{u}\|_2 / \|\mathbf{u}\|_2, \tag{3.7}$$

where

$$\|(\cdot)\|_2 = \sqrt{\int_{-\gamma/2}^{\gamma/2} \int_0^{2\pi} \int_{r_i}^{r_o} (\cdot)^2 r \, dr \, d\theta \, dz}. \tag{3.8}$$

Figure 3 shows that for small Re , $S_{\mathcal{K}} \sim Re^4$. For $Re \lesssim 10$, $S_{\mathcal{K}}$ is essentially machine noise, and for $Re \gtrsim 100$, $S_{\mathcal{K}}$ grows faster than Re^4 , but remains too small for any asymmetry to be evident in figure 1.

4. Instability of the basic state in the axisymmetric subspace

When the meridional flow is sufficiently large ($u, w \gtrsim 0.025v$), S_0 loses stability via a Hopf bifurcation at $Re \approx 575$, and a limit cycle state L_0 is spawned when the dynamics is restricted to the axisymmetric subspace. Figure 4(a) shows how the kinetic energy in S_0 and L_0 varies with Re (for L_0 the time-averaged kinetic energy is shown). For S_0 , $E_0/Re^2 \approx 0.52$ whereas for L_0 the time-averaged scaled kinetic energy drops with increasing Re .

Stratified Taylor–Couette flow: nonlinear dynamics

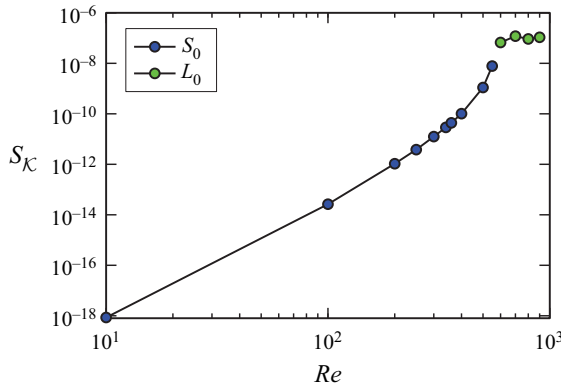


Figure 3. Variation of $S_{\mathcal{K}}$ with Re for the axisymmetric steady state S_0 (blue symbols). For the axisymmetric limit cycle state L_0 (green symbols), the time-averaged $S_{\mathcal{K}}$ is shown.

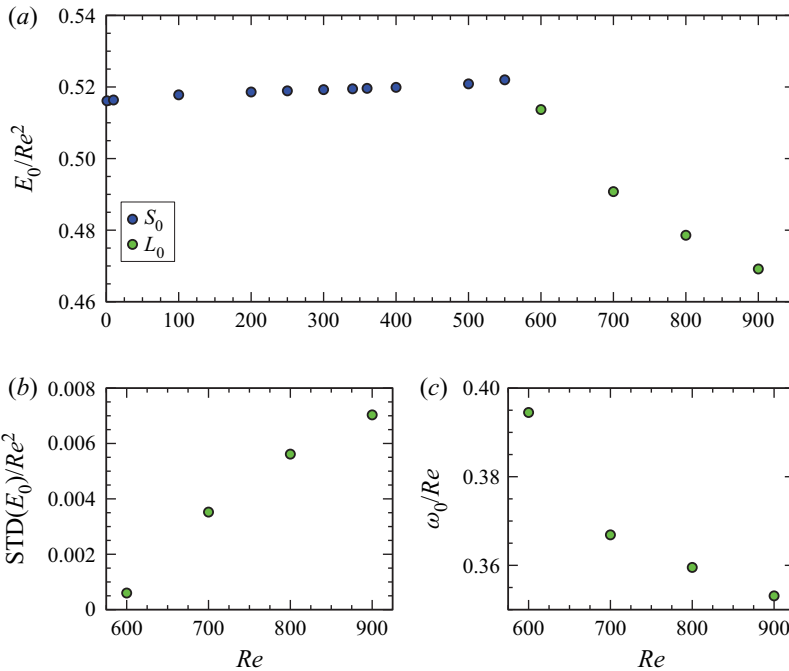


Figure 4. (a) Kinetic energy of solutions computed in the axisymmetric $m = 0$ subspace E_0 , scaled by Re^2 , vs Re . The basic state S_0 is steady, and L_0 is time periodic (for L_0 the time average is plotted). (b) The standard deviation in E_0 , scaled by Re^2 , for L_0 and (c) the corresponding frequency ω_0 scaled by Re , vs Re .

The amplitude of the oscillations in L_0 is quantified by the standard deviation in the time series of the kinetic energy, scaled by Re^2 ; this is shown in figure 4(b). There is near linear growth in the amplitude with increasing Re , starting from zero amplitude at $Re \approx 590$; this is typical of a supercritical Hopf bifurcation. The frequency of the oscillations, scaled by Re , only varies slightly with Re ; this is also typical of a supercritical Hopf bifurcation. This frequency, $\omega_0 \approx 0.36Re$, indicates that the flow oscillates at a frequency that is approximately one third the frequency at which the inner cylinder rotates.

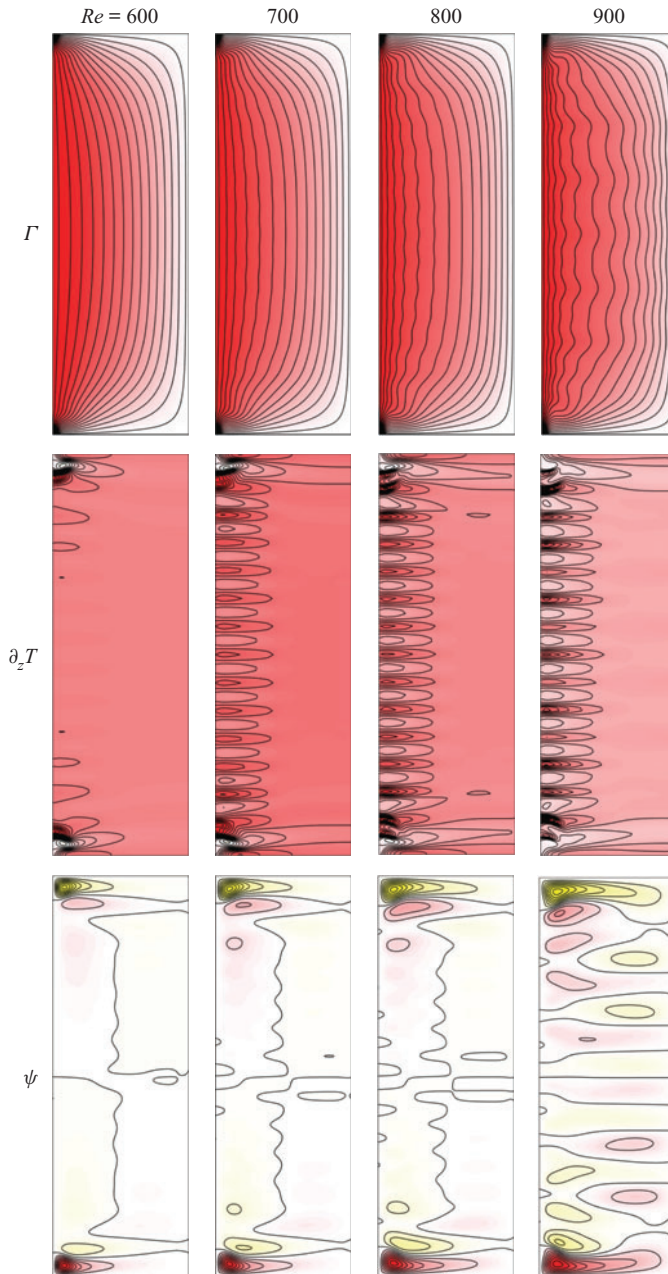


Figure 5. Contours of Γ , $\partial_z T$ and ψ of the time-averaged L_0 at Re as indicated. The contour levels (red positive and yellow negative) are $\Gamma \in [0, r_i Re]$, $\partial_z T \in [0, a]$, where $(Re, a) = (600, 0.700)$, $(700, 0.627)$, $(800, 0.739)$, $(900, 1.032)$ and $\psi \in [-b, b]$, where $(Re, b) = (600, 0.309)$, $(700, 0.510)$, $(800, 0.604)$, $(900, 0.627)$.

Figure 5 shows vortex lines, axial temperature gradient contours and streamlines of L_0 averaged over one period $\tau_0 = 2\pi/\omega_0$ at various Re , from near onset at $Re = 600$ to $Re = 900$. Near onset, the time-average \bar{L}_0 is very similar to the basic state S_0 (compare with S_0 at $Re = 500$ shown in figure 1); the main difference being that there are cellular structures near the inner cylinder that are most intense near the top and bottom endwall corners

and diminishing towards the mid-height region. The time-averaged meridional flow and the deviations away from constant in the time-averaged axial temperature gradients are concentrated in the endwall boundary layers, and in particular near the corners where the endwalls meet the inner cylinder. With increasing Re , the mean meridional flow intensifies, and by $Re = 900$ there is evidence of cellular structure in the interior between the endwalls. The deviations in $\partial_z \bar{T}$ are localized near the inner cylinder, whereas the mean meridional flow extends across the gap between the inner and outer cylinders. This more intense mean meridional flow results in axial oscillations in the mean axial angular momentum $\bar{\Gamma} = r\bar{v}$. For all Re , the mean flow \bar{L}_0 is essentially \mathcal{K} invariant, although very small deviations from \mathcal{K} symmetry are evident, particularly in the streamlines at $Re = 800$ and 900 near the mid-height region.

Figure 6(a,b) shows space–time plots of the angular momentum $\Gamma = rv$ and the axial temperature gradient $\partial_z T$ over four periods of L_0 at $Re = 600$; the oscillation period is $\tau_0 = 2\pi/\omega_0 \approx 15.93Re$. Figure 6(c,d) shows snapshots of Γ and $\partial_z T$ at eight equispaced times in one period, indicated by the vertical dashed blue lines in the space–time plots. The instantaneous L_0 has a well-defined interior cellular structure (see snapshots at t_0), but this cellular structure becomes weaker and almost disappears after a quarter period (see snapshots at $t_0 + \tau_0/4$), and reappears again after another quarter period (see snapshots at $t_0 + \tau_0/2$), but with the cellular structure being the \mathcal{K} -symmetric conjugate of the cellular structure at t_0 . This cycle repeats with period τ_0 . This is the reason why the number of cellular structures in the time-average \bar{L}_0 (figure 5) is twice the number of cells in L_0 (figure 6d): the cells at t_0 superimposed with the z -reflected cells at $t_0 + \tau_0/2$ results in doubling the number of cells in the time average. The space–time plots show that the cells are formed at the endwalls and move towards the interior, meeting at the mid-height level. Figure 6 clearly shows that the \mathcal{K} symmetry at any given time is broken. However, there is an almost perfect half-period-flip symmetry: the snapshots after half a period $t + \tau_0/2$ coincide with the \mathcal{K} -conjugate snapshots at t (for any t), as discussed earlier. A Hopf bifurcation caused by a pair of complex conjugate antisymmetric eigenvectors typically/generically leads to a limit cycle which has this half-period-flip symmetry. Strictly speaking, since the centrifugal term breaks the \mathcal{K} symmetry, there are slight differences that cannot be appreciated in the figure because the breaking of the \mathcal{K} symmetry at this low Reynolds number ($Re = 600$) is extremely small ($S_{\mathcal{K}} \sim 10^{-7}$, as shown in figure 3).

Figure 7 shows the corresponding plots from figure 6 for L_0 at $Re = 800$. It is evident that instead of having an approximate half-period-flip symmetry (i.e. setwise \mathcal{K} invariance), the flow at this Re is pointwise-in-time \mathcal{K} invariant. This type of switching between stable limit cycles bifurcating from a basic state with \mathcal{K} symmetry to periodic states that either have pointwise-in-time \mathcal{K} symmetry (L_0 at $Re = 800$) or setwise-in-time (half-period-flip) symmetry (L_0 at $Re = 600$) is commonly observed in \mathcal{K} (or related Z_2) symmetric systems (e.g. Marques & Lopez 2015; Yalim, Welfert & Lopez 2019; Grayer *et al.* 2020). Strictly speaking, in the present problem the \mathcal{K} symmetry is broken due to the centrifugal buoyancy, as has already been discussed. This symmetry breaking is very weak, but at $Re = 800$, a close inspection of some of the snapshots in figure 7(d) near the mid-height shows clear evidence of the symmetry breaking. The cellular structures at $Re = 800$ are more pronounced than at $Re = 600$ as L_0 is further away from onset.

While the snapshots in figures 6 and 7 are instructive, the animations of the fields (see supplementary movie 1 available at <https://doi.org/10.1017/jfm.2021.893>) illustrate the dynamics better. Twice every period, a new cell is formed at each of the corners where the endwalls meet the inner cylinder. The new cells propagate axially into the interior, pushing the existing cells further toward the mid-plane $z = 0$, resulting in the

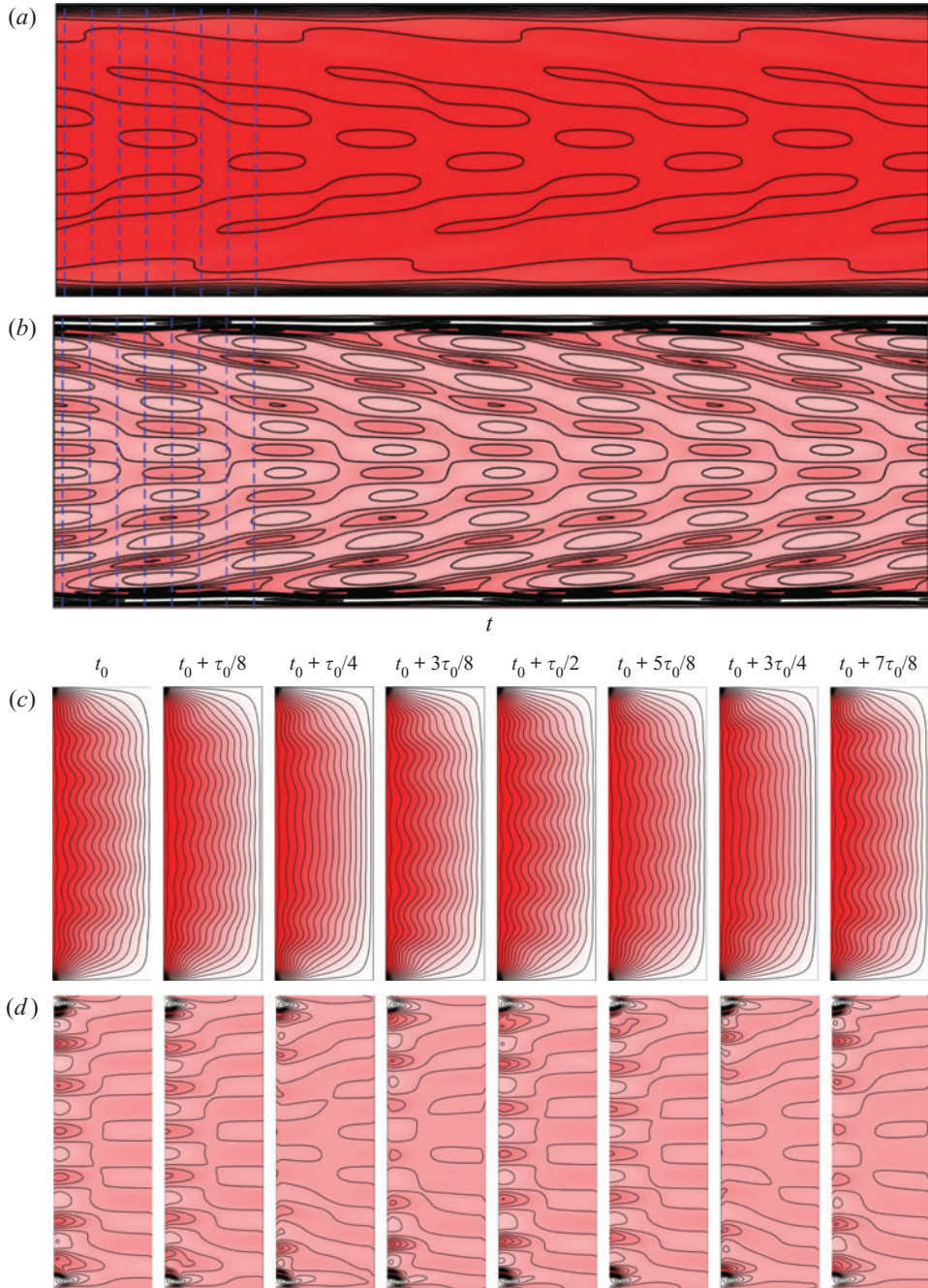


Figure 6. The limit cycle L_0 at $Re = 600$: space–time (t, z) contour plots of (a) Γ and (b) $\partial_z T$ at $\theta = 0$ and $r = r_i + 0.1$; four periods are shown, where $\tau_0 = 2\pi/\omega_0 \approx 15.92/Re$ is the period of L_0 . The corresponding meridional snapshots at indicated times corresponding to the eight equispaced vertical dashed blue lines in (a,b) are shown in (c,d). Supplementary movie 1 animates the Γ and $\partial_z T$ contours in the meridional plane over one period.

annihilation of the angular momentum jets and cells. The jets reappear in other places, with either the same or a different number of cells, depending on the symmetry of L_0 . Jets of angular momentum, which are characteristic of the centrifugal instability due to the

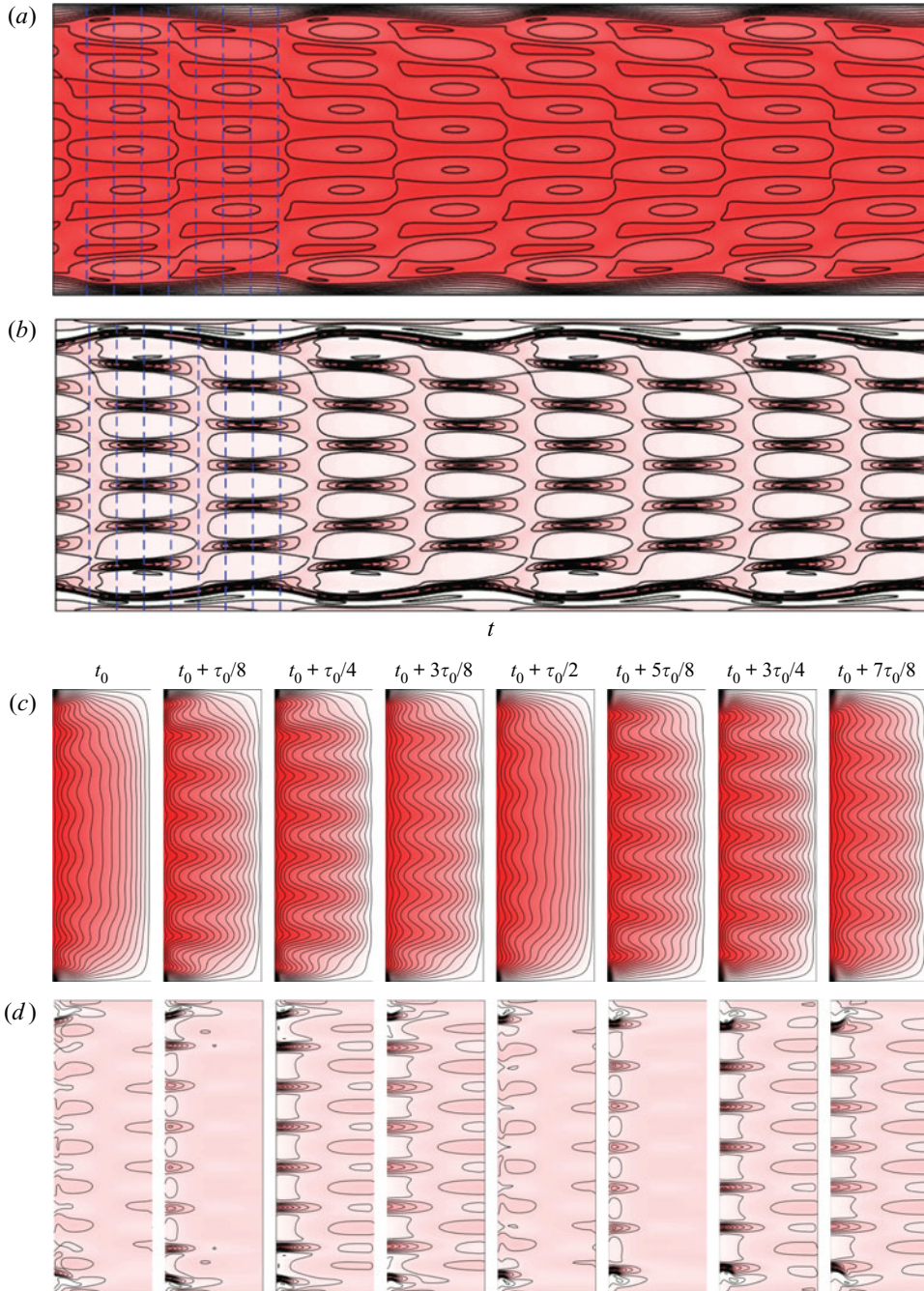


Figure 7. The limit cycle L_0 at $Re = 800$: space–time (t, z) contour plots of (a) Γ and (b) $\partial_z T$ at $\theta = 0$ and $r = r_i + 0.1$; four periods are shown, where $\tau_0 = 2\pi/\omega_0 \approx 17.67/Re$ is the period of L_0 . The corresponding meridional snapshots at indicated times corresponding to the eight equispaced vertical dashed blue lines in (a,b) are shown in (c,d). Supplementary movie 1 animates the Γ and $\partial_z T$ contours in the meridional plane over one period.

inner cylinder rotation, are clearly observed. During a period, these jets intensify, become weaker, disappear and then reappear with their radial direction inverted, i.e. the outgoing jets become ingoing jets and *vice versa* (see, for example, the snapshots in figure 7c at times

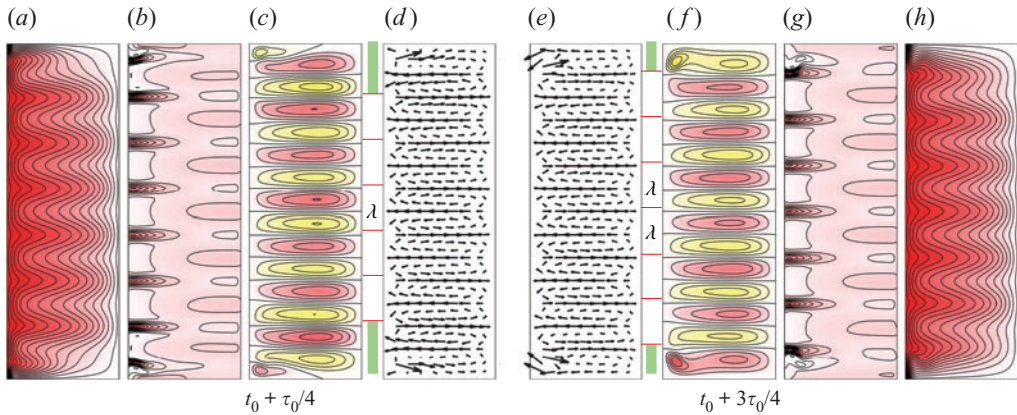


Figure 8. The limit cycle L_0 at $Re = 800$, showing Γ , $\partial_z T$, ψ and velocity vectors projected onto a meridional plane at two times, (a,b,c,d) and (h,g,f,e), half a period apart, during which the outgoing radial jets are strongest.

$t_0 + \tau_0/4$ and $t_0 + 3\tau_0/4$). There is a pair of counter-rotating Taylor vortices between two adjacent outgoing jets, forming a Taylor cell, as illustrated in figure 8(d,e), showing the meridional velocity field of L_0 at $Re = 800$, at the two times $t_0 + \tau_0/4$ and $t_0 + 3\tau_0/4$, when the jets are most intense. Instantaneous streamlines, axial temperature gradient and angular momentum contours are also shown in the figure, and movie 1 animates these over one period.

The Taylor cell boundaries (i.e. the outgoing jets) are indicated by red lines in figure 8. These boundaries are flat, except near the endwalls where the intense Ekman layers with strong velocities near the corners at the inner cylinder distort the adjacent cell boundaries. Each Taylor cell consists of a pair of counter-rotating Taylor vortices. The axial wavelength λ (i.e. the axial height of the Taylor cell relative to the annular gap) is invariant along the cylinder (except very near the Ekman layers), and it remains unchanged in time, even following the switching between ingoing and outgoing jets. This wavelength is much smaller than the wavelength of Taylor cells in unstratified Taylor-vortex flow, which typically have $\lambda_{TVF} \sim 2$ (the Taylor vortices tend to have a square cross-section). Since the flow is divergence free, the strong radial flows in the cells must have axial components to complete the circuits, but the stratification tends to inhibit axial flow, and so the axial flow is constrained to the boundary layers on the inner and outer cylinders. The axial flow on the inner cylinder, together with the radial flow there, leads to the isotherms being advected to the borders of the cells such that where the axial flow converges at these borders, the isotherms are concentrated axially, resulting in a step-like layering. For L_0 at $Re = 800$, $\lambda \approx 0.415$; the stratification inhibits the axial motions and reduces the axial span of the cells to approximately $1/5$ of λ_{TVF} .

The outgoing jets are associated with intense axial temperature gradients, as shown in figure 8. Figure 7(b) shows a space–time plot of $\partial_z T$; the white ovals are regions of constant temperature ($\partial_z T = 0$), separated by narrow axial regions of large axial temperature gradients, corresponding to the narrow radial ‘jets’ of $\partial_z T$ in figure 8. The temperature has a ‘staircase’ structure (step-like layering) near the inner cylinder (between the inner cylinder and the mid-gap), with regions of constant temperature (the Taylor cells) separated by narrow regions of large axial temperature gradient coinciding with the centres of the outgoing jets. The stratification changes periodically with time and the layering appears and disappears periodically in different axial locations. These step-like

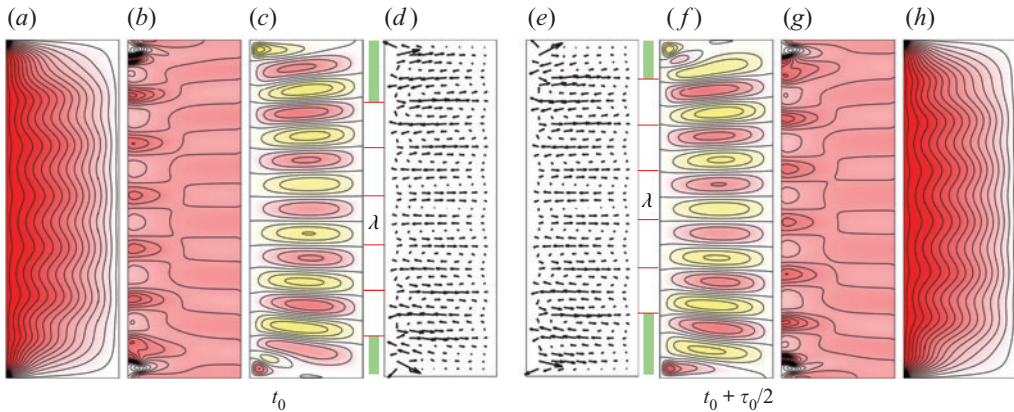


Figure 9. The limit cycle L_0 at $Re = 600$ showing Γ , $\partial_z T$, ψ and velocity vectors projected onto a meridional plane at two times, (a,b,c,d) and (h,g,f,e), half a period apart, during which the outgoing radial jets are strongest.

layers are confined near the cylinder; this is the region where the centrifugal instability mechanism is most active. The layering does not have time to propagate radially out to the outer cylinder due to the temporal oscillations of the jets. During the short time intervals when the angular momentum jets disappear, the temperature stratification becomes mostly uniform in the axial direction, as shown in [figure 7](#).

The switching between ingoing and outgoing jets results in a different number of Taylor cells, changing between 5 and 6 cells for L_0 at $Re = 800$. The cell boundaries are indicated by red lines in [figure 8](#). The axial size of the cells, λ , does not vary during the switching: the Ekman vortices at the endwalls change size in order to accommodate a different number of cells. The size of the Ekman vortices is indicated in green in [figure 8](#). When the Ekman vortex is large, it develops an outgoing jet of angular momentum in its interior that propagates axially from the endwall, resulting in the switching between different number of cells.

When the Ekman layer is small ([figure 8e](#)) the radial velocity at the endwalls is inwards. This is what has been called in many studies of Taylor–Couette flow a normal mode (Benjamin & Mullin 1981; Cliffe *et al.* 1992; Watanabe, Furukawa & Nakamura 2002; Lopez & Marques 2005; Marques & Lopez 2006). When the Ekman layer is large ([figure 8d](#)) the radial velocity at the endwalls is outwards, as in a so-called anomalous mode. This switching is typical of many Taylor–Couette flows of finite axial extent. For L_0 at $Re = 800$, the switching between normal and anomalous mode types occurs twice every oscillation period. It is worth mentioning that even during the anomalous mode phase, there is still a small corner vortex near the inner cylinder so that the radial velocity is locally inwards ([figure 8d](#)).

We have described the flow of L_0 at $Re = 800$ in more detail than that of L_0 at $Re = 600$ because the jets, cellular structures and staircase temperature profiles are much more evident. In [figure 9](#) for L_0 at $Re = 600$ we observe similar cellular structures, and jets of angular momentum as at $Re = 800$. However, due to the different symmetry of the flow, the behaviour of the Ekman cells is different. In the $Re = 800$ case, with \mathcal{K} symmetry, both Ekman layers have the same size and when their size changes, the number of cells also changes. In the $Re = 600$ case, when one of the Ekman layers grows, the other shrinks, and as a result the number of cells does not change. The cells become weaker, disappear, and then reappear with the radial direction of the jets inverted, as in the

$Re = 800$ case. For $Re = 600$, there is just an axial oscillation of the cells, combined with their formation/vanishing. The wavelength is constant all the time, $\lambda \approx 0.423$. Compared with the $Re = 800$ case ($\lambda \approx 0.415$) we see that the cell size does not change very much with Re , there is a small decrease in λ with increasing Re . Also, for the half-period-flip symmetric L_0 at $Re = 600$, one Ekman layer is in the normal mode phase while the other is in the anomalous mode phase. There is still a pair of persistent corner vortices maintaining the radial flows into the corner on both endwalls.

5. Three-dimensional instability of the basic state

In the previous section, the primary instability of the basic state S_0 was explored by restricting the flow to the axisymmetric subspace. Without making such a restriction, S_0 loses stability at a lower $Re \approx 320$ via a Hopf bifurcation breaking the $SO(2)$ symmetry, leading to a rotating wave with azimuthal wavenumber $m = 1$, denoted R_1 . Figure 10(a) shows how the modal kinetic energy in $m = 1$, scaled by Re^2 , increases linearly from zero at onset and saturates nonlinearly by $Re \approx 700$. For $Re \gtrsim 1000$, the rotating wave has a low-amplitude long-period irregular modulation (this modulated rotating wave, MR_1 , is described below). For MR_1 , the reported modal energies are time averaged. Figure 10(b) shows the scaled modal kinetic energy in the axisymmetric component of the flow, E_0/Re^2 . It is two orders of magnitude larger than E_1/Re^2 . For the rotating waves, E_1/Re^2 is a measure of their amplitude, just as the scaled standard deviation in E_0 was a measure of the oscillation amplitude of L_0 (figure 4b); these two amplitudes are of comparable magnitude. Figure 10(c) shows the precession frequency of the rotating wave scaled by Re , ω_p/Re . It decreases slowly with increasing Re , but remains close to one third of the rotation frequency of the inner cylinder. This is similar to the behaviour of the oscillation frequency ω_0 of L_0 (see figure 4c), but ω_p is a little smaller than ω_0 overall.

For the small Re at which the Hopf bifurcation spawning R_1 occurs when $Fr \approx 0.53$, the imperfection in the \mathcal{K} symmetry about the axial mid-plane is essentially negligible; $S_{\mathcal{K}} = 2.9 \times 10^{-11}$ for the base state S_0 at $Re = 340$. Along with the $SO(2)$ symmetry, the \mathcal{K} symmetry is also broken at the bifurcation leading to a rotating wave R_1 that has centrosymmetry (albeit imperfect due to $\epsilon \approx 2.4 \times 10^{-4}$ being small but not zero). The action of centrosymmetry, $\mathcal{C} = \mathcal{R}_\pi \mathcal{K} = \mathcal{K} \mathcal{R}_\pi$, is

$$\mathcal{C} : [u, v, w, T](r, \theta, z, t) \mapsto [u, v, -w, -T](r, \theta - \pi, -z, t), \tag{5.1}$$

and for a rotating wave with azimuthal wavenumber $m = 1$ and precession frequency ω_1 ,

$$[u, v, w, T](r, \theta - \phi, z, t) = [u, v, w, T](r, \theta, z, t + \phi/\omega_1). \tag{5.2}$$

For a rotating wave, the centrosymmetry \mathcal{C} is the same as the half-period-flip symmetry because a rotation of π is the same as advancing half a period in time. As a quantitative measure of the \mathcal{C} centrosymmetry, we introduce the symmetry measure

$$S_{\mathcal{C}} = \|\mathbf{u} - \mathcal{C}\mathbf{u}\|_2 / \|\mathbf{u}\|_2. \tag{5.3}$$

Figure 10(d) shows the symmetry measures $S_{\mathcal{K}}$ and $S_{\mathcal{C}}$ of R_1 and MR_1 . For the rotating waves at $Re \leq 1000$, one or the other symmetry measure is very small (of order 10^{-6}) while the other grows from near zero to 0.2 with increasing Re . The rotating wave R_1 comes in two flavours, one \mathcal{C} symmetric and the other \mathcal{K} symmetric, and alternates between the two cases as Re is increased. This is analogous to switching between setwise and pointwise-in-time \mathcal{K} invariance for the axisymmetric limit cycle L_0 . The \mathcal{C} symmetry is the purely spatial version of the half-period-flip symmetry. It is very likely that the underlying

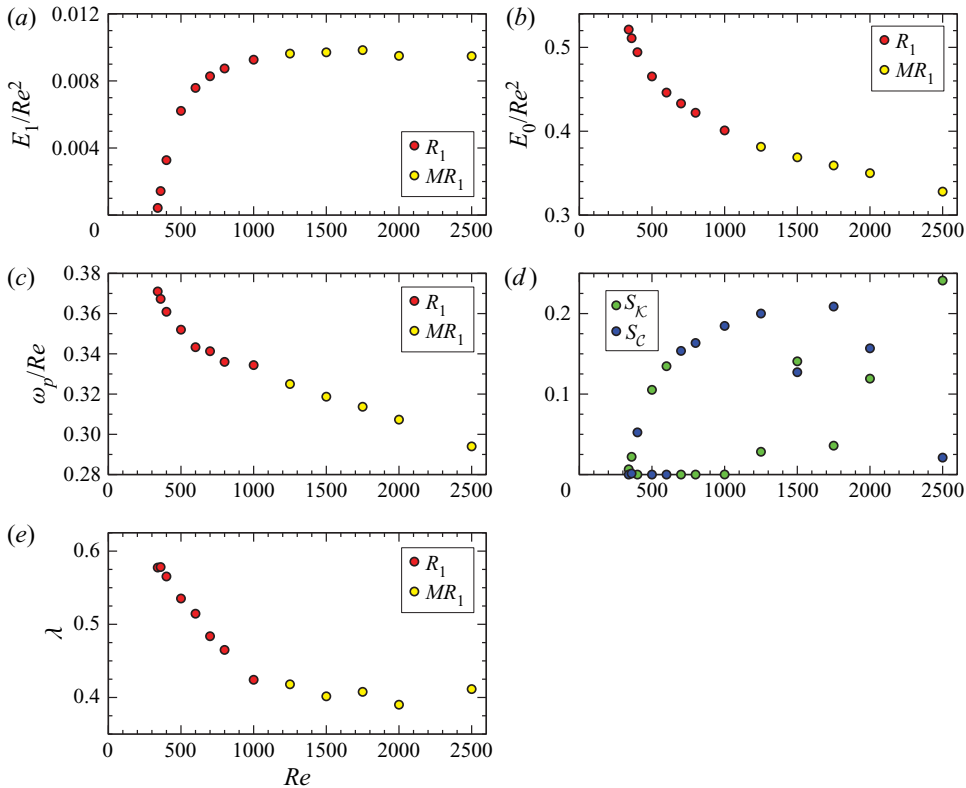


Figure 10. Variation with Re of the scaled modal kinetic energies in azimuthal wavenumber (a) $m = 1$, E_1/Re^2 and (b) $m = 0$, E_0/Re^2 , (c) the scaled precession frequency ω_p/Re of the rotating wave R_1 (red symbols) and modulated rotating waves MR_1 (yellow symbols), all for $Fr \approx 0.53$. (d) The symmetry measures S_K and S_C of these states, and (e) axial wavelength, λ , measured at $r = r_i + 0.1$ near mid-height $z = 0$.

mechanisms for the symmetry-type switching with increasing Re in L_0 and R_0 are the same, and tied to the underlying \mathcal{K} symmetry of the basic state S_0 .

Figure 10(e) shows the variation of the axial wavelength λ of the Taylor cells. It is measured as the distance between the peaks of azimuthal temperature gradient $\partial_z T$ closest to mid-height $z = 0$ (i.e. away from the endwalls and the distorting effects of the Ekman vortices), near the inner cylinder (at $r = r_i + 0.1$). Figure 8 shows a typical example for L_0 , illustrating where λ has been measured. The wavelength λ steadily decreases linearly with Re for R_1 (except for the first point very near the bifurcation $Re \approx 340$, where the Taylor cells are weak and λ is difficult to measure). In contrast, for $Re > 1000$ the wavelength of the modulated rotating waves MR_1 remains almost independent of Re with $\lambda \sim 0.4$.

Figure 11(a,b) shows space–time plots of Γ and $\partial_z T$ along an axial line at $(r, \theta, z) = (r_i + 0.1, 0, z)$ over four precession periods of R_1 at $Re = 500$; the precession period is $\tau_p = 2\pi/\omega_p \approx 17.85Re$. These space–time plots can also be viewed as (θ, z) plots because R_1 is a rotating wave (the time $t \in [t_0, t_0 + 4\tau_p]$ being replaced with $\theta \in [0, 8\pi]$). The figure shows the same features as in the space–time plots for L_0 : there are regions of constant temperature (white regions in figure 11a) bounded in z by regions of large axial temperature gradient – the staircase temperature profiles described earlier for L_0 . Figure 11(c,d) shows snapshots, in the meridional plane $\theta = 0$, of Γ and $\partial_z T$ at eight equispaced times over one period (or equivalently, in eight equispaced meridional planes

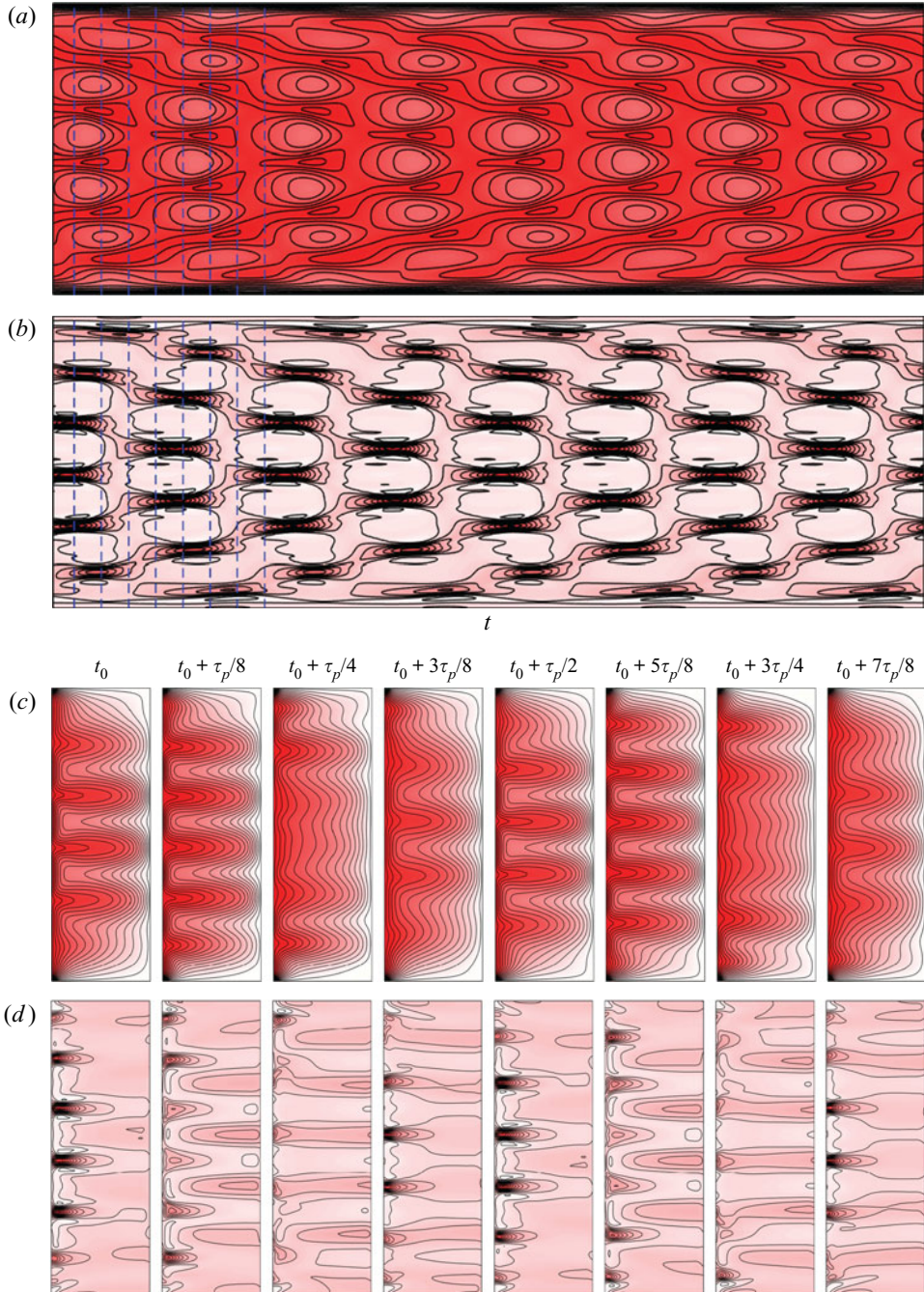


Figure 11. The rotating wave R_1 at $Re = 500$: space–time (t, z) contour plots of (a) Γ and (b) $\partial_z T$ at $\theta = 0$ and $r = r_i + 0.1$; four precession periods are shown, where $\tau_p = 2\pi/\omega_p \approx 17.85/Re$ is the precession period of R_1 . The corresponding meridional snapshots at indicated times corresponding to the eight equispaced vertical dashed blue lines in (a,b) are shown in (c,d).

with $\theta \in [0, 2\pi]$, all at the same instant in time), indicated by the vertical dashed blue lines in the space–time plots. The rotating wave R_1 at $Re = 500$ is essentially \mathcal{C} symmetric ($S_{\mathcal{C}} = 4.14 \times 10^{-6} \approx 0$ and $S_{\mathcal{K}} = 0.105 \neq 0$). The outgoing jets of angular momentum,

coinciding with the regions of large axial temperature variation, are clearly evident. Over one period in a particular meridional plane, these jets become weaker, disappear and then reappear with the direction of their radial velocity reversed. However, for R_1 these structures remain invariant in time and simply rotate continuously in azimuth. In contrast, for L_0 the formation and destruction of the jets and sharp axial temperature gradients occurs globally in azimuth and periodically in time. The R_1 jets are essentially θ -invariant for $\theta_0 \lesssim \theta \lesssim \theta_0 + \pi$ and for $\theta_0 + \pi \lesssim \theta \lesssim \theta_0 + 2\pi$, but displaced axially by $\lambda/2$ in the two azimuthal halves, with narrow bands of ‘defects’ connecting the jets in the two halves.

Figure 12(a,b) shows space–time plots of Γ and $\partial_z T$ over four precession periods of R_1 at $Re = 800$; the precession period is $\tau_p = 2\pi/\omega_p \approx 18.65Re$. Figure 12(c,d) shows snapshots of Γ and $\partial_z T$ at eight equispaced times in one period, indicated by the vertical dashed blue lines in the space–time plots. The value of R_1 at $Re = 800$ is essentially \mathcal{K} symmetric ($S_{\mathcal{K}} = 2.14 \times 10^{-5} \approx 0$ and $S_{\mathcal{C}} = 0.163 \neq 0$). The same considerations as for R_1 at $Re = 500$ apply here, the only difference being the different symmetry of the solution. Figure 13 shows snapshots of Γ and $\partial_z T$ isosurface, one quarter period apart, illustrating the three-dimensional structure of R_1 at $Re = 500$ and 800 . Supplementary movie 2 shows animations of these over one precession period; these animations provide clearer insights into the flow structures.

Figure 14 shows vortex lines, axial temperature gradient contours and streamlines of R_1 averaged over one period $\tau_0 = 2\pi/\omega_0$ (or equivalently, averaged with respect to θ) at various Re , from near onset at $Re = 340$ to $Re = 1000$. The plots are very similar to those in figure 5 for the time-averaged L_0 . The only significant difference is that the cellular structures are more intense and the jets of angular momentum (and the associated staircase structures in the temperature) penetrate radially further in from the inner cylinder for R_1 than they do for L_0 .

For $Re > 1000$, centrifugal buoyancy effects are stronger, leading to greater asymmetry between the two rotating waves associated with the upper and lower corners. They now have slightly different precession frequencies, resulting in a quasiperiodic modulated rotating wave, MR_1 . The modulation is a very low frequency beating on the underlying rotating wave. Figure 15 shows time series of the modal kinetic energy E_1 scaled by Re^2 and the corresponding power spectral densities for R_1 at $Re = 1000$ and MR_1 at a selection of larger Re . They clearly show the appearance of a very low frequency ω_2 . More importantly, the primary peak is associated with the precession frequency of the underlying rotating wave, $\omega_p \approx 0.32$ with a very small decrease with increasing Re ; the power in this primary peak is almost two orders of magnitude larger than the power in the very low frequency modulation peak. As such, the modulations are weak and manifest over hundreds of inner cylinder rotations.

Figure 16 shows space–time plots of Γ and $\partial_z T$ over four precession periods for R_1 at $Re = 1000$ and MR_1 at a selection of larger Re . The main feature of these spatio-temporal structures is the presence of the staircase structures, with very narrow regions of fast variation of temperature, separated by regions of almost constant temperature, as shown in the second column of figure 16. These structures, and the associated outgoing jets of angular momentum, are distorted with increasing Re , and the \mathcal{C} and \mathcal{K} symmetries are completely broken. The propagation towards the interior of the perturbations generated at each endwall is clearly evident. Some of the plots show that the waves propagating from the top endwall fill most of the interior (as in figure 16b for $Re = 1250$), and others show the opposite (as in figure 16c for $Re = 1500$). In fact, the dominance of one or other of the endwalls changes very slowly in time, corresponding to the very low frequency ω_2

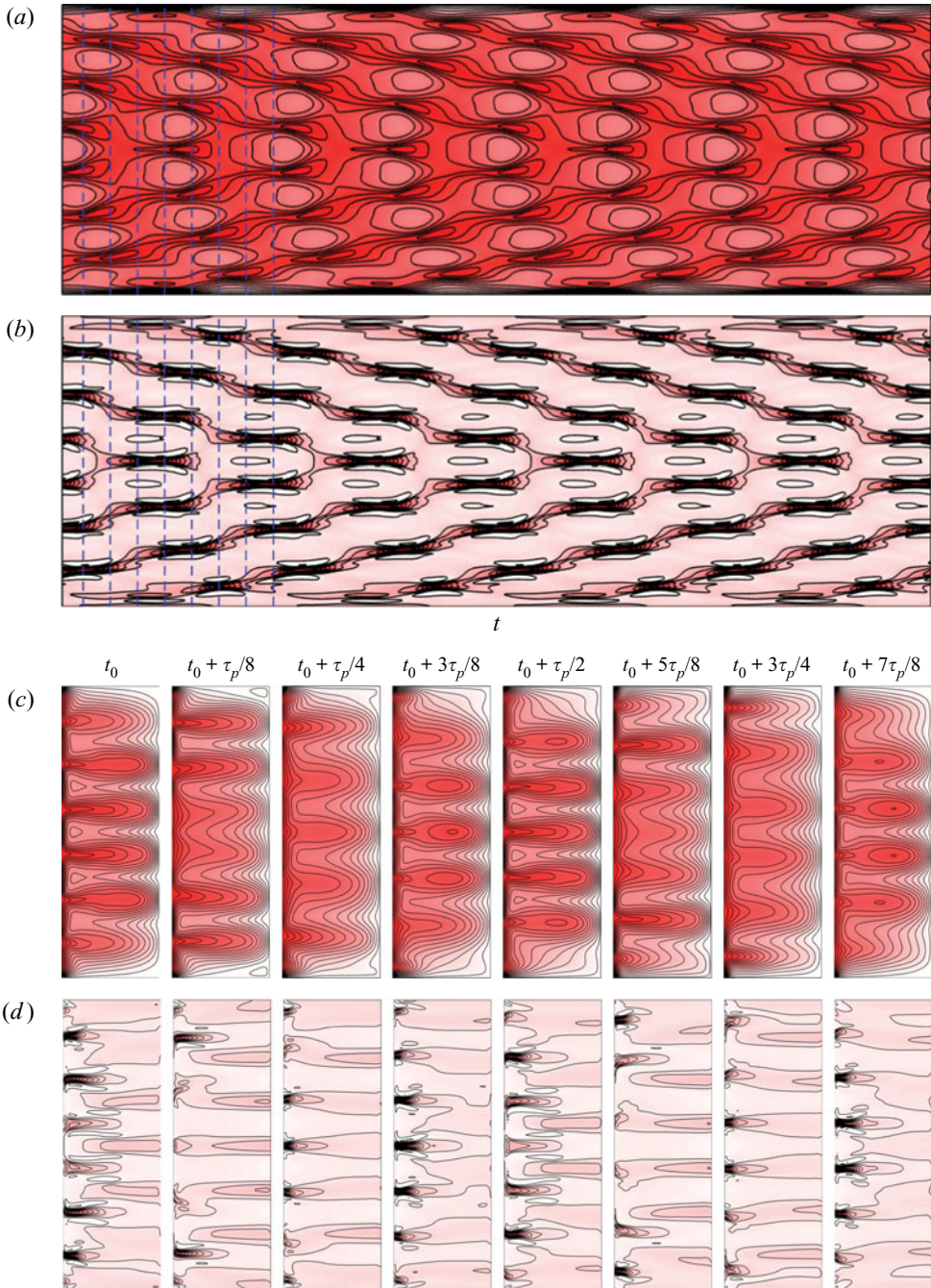


Figure 12. The rotating wave R_1 at $Re = 800$: space-time (t, z) contour plots of (a) Γ and (b) $\partial_z T$ at $\theta = 0$ and $r = r_i + 0.1$; four precession periods are shown, where $\tau_p = 2\pi/\omega_p \approx 18.65/Re$ is the period of R_1 . The corresponding meridional snapshots at indicated times corresponding to the eight equispaced vertical dashed blue lines in (a,b) are shown in (c,d).

of MR_1 . This is due to the detuning between the oscillation frequencies of the Ekman vortices at the endwalls. This type of behaviour was also observed in Lopez & Marques (2020), with smaller radius ratio and larger stratification. The spatio-temporal plots in

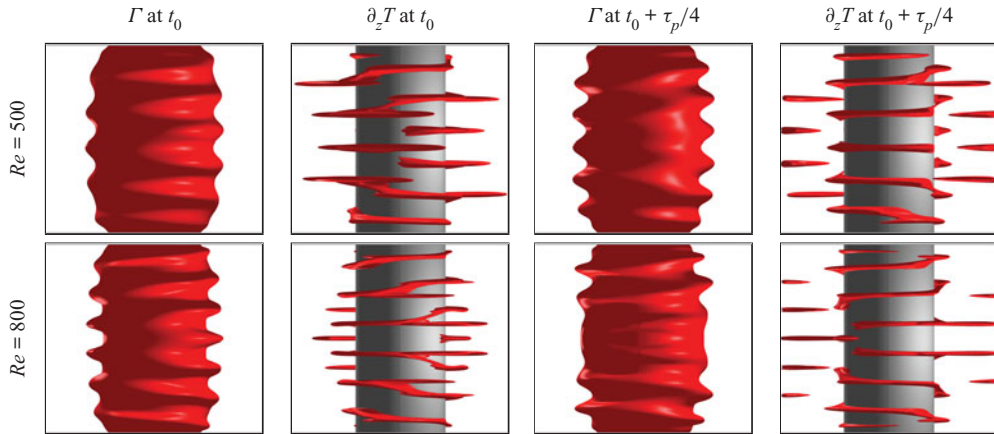


Figure 13. Isosurfaces of Γ and $\partial_z T$ of R_1 at $Re = 500$ and 800 , at two different times a quarter precession period apart. The isolevels are $\Gamma = 0.4r_i Re$ and $\partial_z T = 0.493$ (which is 30 % of the maximum axial temperature gradient) for $Re = 500$ and $\partial_z T = 0.625$ (which is 22 % of the maximum axial temperature gradient) for $Re = 800$. Supplementary movie 2 includes an animation of these over one precession period.

figure 16 are also very similar to those reported from experiments using salt stratification in a Taylor–Couette apparatus with very similar radius and aspect ratios (Partridge *et al.* 2016), as well as in experiments using temperature stratification with oil and quite larger radius ratio $\eta \approx 0.52$ and aspect ratio $\gamma \approx 10$ (Meletti *et al.* 2021). This suggests that the Prandtl number (which varies from approximately 700 for salt stratification, approximately 57 for the oil, to approximately 6 for temperature stratification in water) does not play a critical role in the layering pattern selection process.

Figure 17 illustrates the changes in flow structure associated with the very low frequency $\omega_2 \approx \omega_p/20$ for MR_1 at $Re = 1250$. It includes time series of the axial velocity w at three points in a meridional plane, $\theta = 0$, very close to the inner cylinder, $r = r_i + 0.01$, at three heights, $z = 0$ and $z = \pm 0.5\gamma$, as well as time series of the symmetry measures S_C and S_K . The time series are shown over one viscous time, which is approximately three times $2\pi/\omega_2$. Over most of each $2\pi/\omega_2$ period, the flow has a regular almost periodic behaviour during which it is approximately \mathcal{K} -symmetric ($S_K \approx 0$). As a consequence, the axial velocity w at $z = 0$ is approximately zero and $w|_{z=0.5\gamma} \approx -w|_{z=-0.5\gamma}$. This regular, nearly \mathcal{K} -symmetric phase is followed by an irregular shorter phase during which the reflection symmetry measure S_K increases to be approximately a fifth of S_C ; S_C also increases ever so slightly during this phase. The yellow symbols in the time series in figure 17 are strobed with the precession frequency ω_p , and the isosurfaces of $\partial_z T$ at these strobed times are shown in supplementary movie 3. Fifteen equispaced snapshots (five per period $2\pi/\omega_2$) are shown in figure 17(f). The first three snapshots in each row (each row covers one $2\pi/\omega_2$ period) show very little variation, corresponding to the regular phase of MR_1 , with almost ω_p -periodic behaviour. The last two snapshots correspond to the irregular phase, with rapid changes in the flow. The (strobed) position of the defect at mid-height remains constant during the regular phase, while it experiences a jump during the irregular phase; this jump coincides with \mathcal{K} -symmetry breaking. This behaviour is a ‘snapping’ of the defect; it was also observed in very wide-gap stratified Taylor–Couette flow (Lopez & Marques 2020), in which both curvature and centrifugal buoyancy effects were much stronger than in the present problem. There, the ‘snapping’ was related to the detuning of the frequencies associated with the centrifugal instabilities near the endwalls.

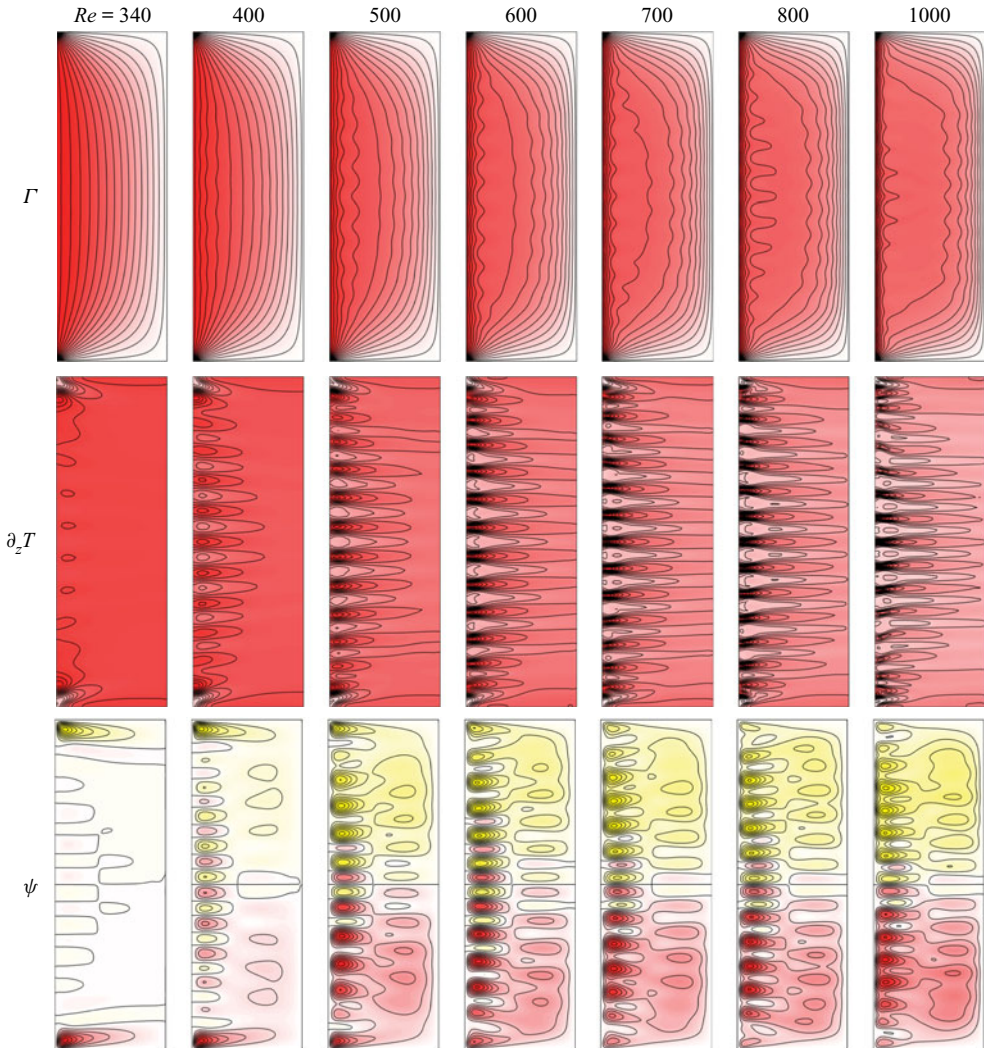


Figure 14. Contours of Γ , $\partial_z T$ and ψ of the time-averaged R_1 at Re as indicated. The contour levels (red positive and yellow negative) are $\Gamma \in [0, r_i Re]$, $\partial_z T \in [0, 0.2 + 7.5 \times 10^{-4} Re]$ and $\psi \in [-b, b]$, where $b = -0.09 + 2.3 \times 10^{-5} Re^{3/2}$.

This effect was large in that study, and affected the first instability of the flow. In the present problem, centrifugal buoyancy effects begin to manifest well beyond the onset of instability (for $Re > 1000$ compared with onset at $Re \approx 320$), and result in the transition to modulated rotating waves MR_1 . Further increases in Re above $Re \approx 2000$ results in complex spatio-temporal behaviour, as the time series and power spectral densities in [figure 15](#) indicate.

6. Discussion and conclusions

We have presented a detailed study of the onset of instability of stratified Taylor–Couette flow in an annulus with medium radius ratio, $\eta = 0.417$, and short aspect ratio, $\gamma = 3$,

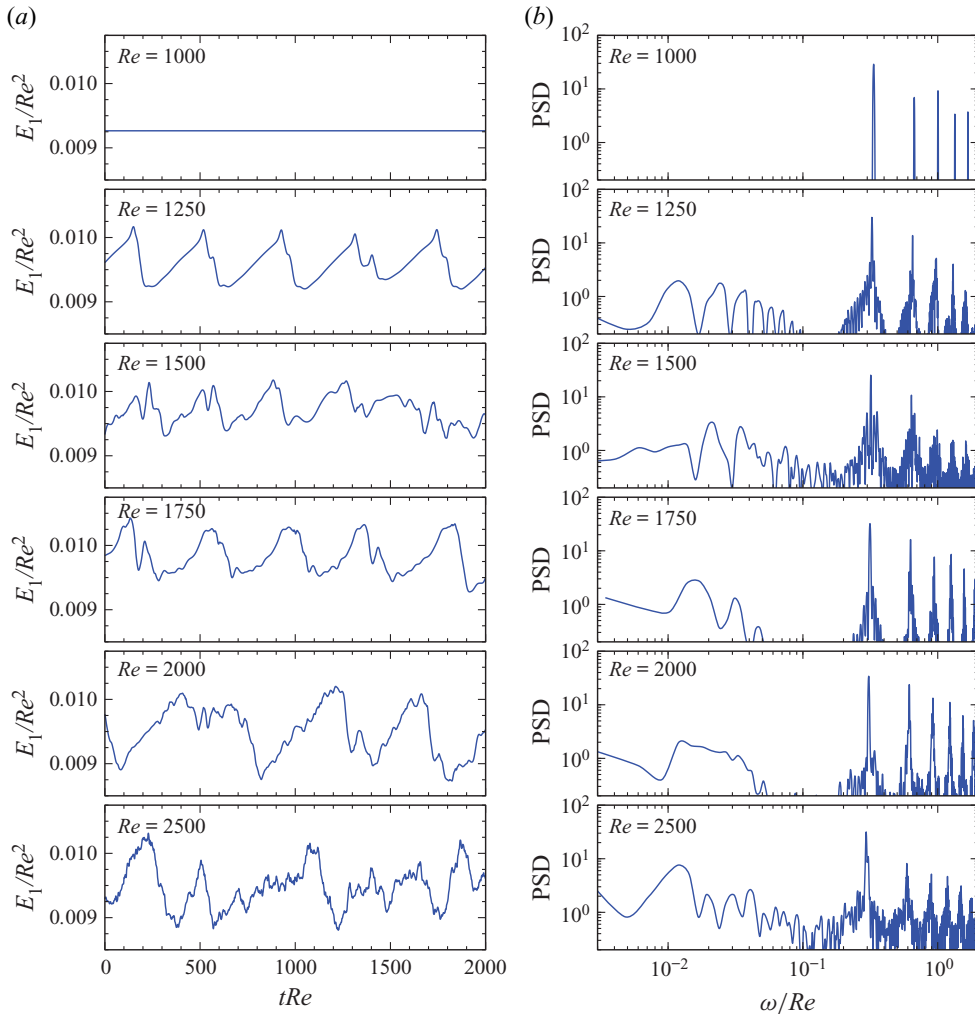


Figure 15. Time series (a) of the modal kinetic energy E_1/Re^2 , and (b) power spectral density (PSD) of the azimuthal component of velocity at a point $(r, \theta, z) = (r_i + 0.1, 0, 0.25\gamma)$, for $Fr \approx 0.53$ and Re as indicated.

inspired by a series of experiments (Oglethorpe *et al.* 2013; Leclercq *et al.* 2016b,d; Partridge *et al.* 2016). This is a very different geometry to that usually studied, where the aspect ratio is large to minimize endwall effects and the radius ratio is large ($\eta \sim 1$) to minimize curvature effects (e.g. Boubnov *et al.* 1995; Le Bars & Le Gal 2007; Ibanez *et al.* 2016). As in unstratified Taylor–Couette flow in a finite annulus, the instability initiates at the corners where the inner rotating cylinder meets the stationary endwalls. From there, it propagates axially into the interior along the inner cylinder. This process is (up-down) \mathcal{K} symmetric in the absence of stratification. However, with stratification the centrifugal buoyancy breaks the \mathcal{K} symmetry, albeit weakly near onset of instability for the parameter regimes considered in this study.

In similar stratified Taylor–Couette flows with smaller radius ratio, $\eta \approx 0.07$, and stronger stratification (Flór *et al.* 2018; Lopez & Marques 2020), the corner vortices emit spiral waves with small inclination towards the interior. The frequencies of these spiral waves emitted from the top and bottom endwalls are slightly different due to the imperfect

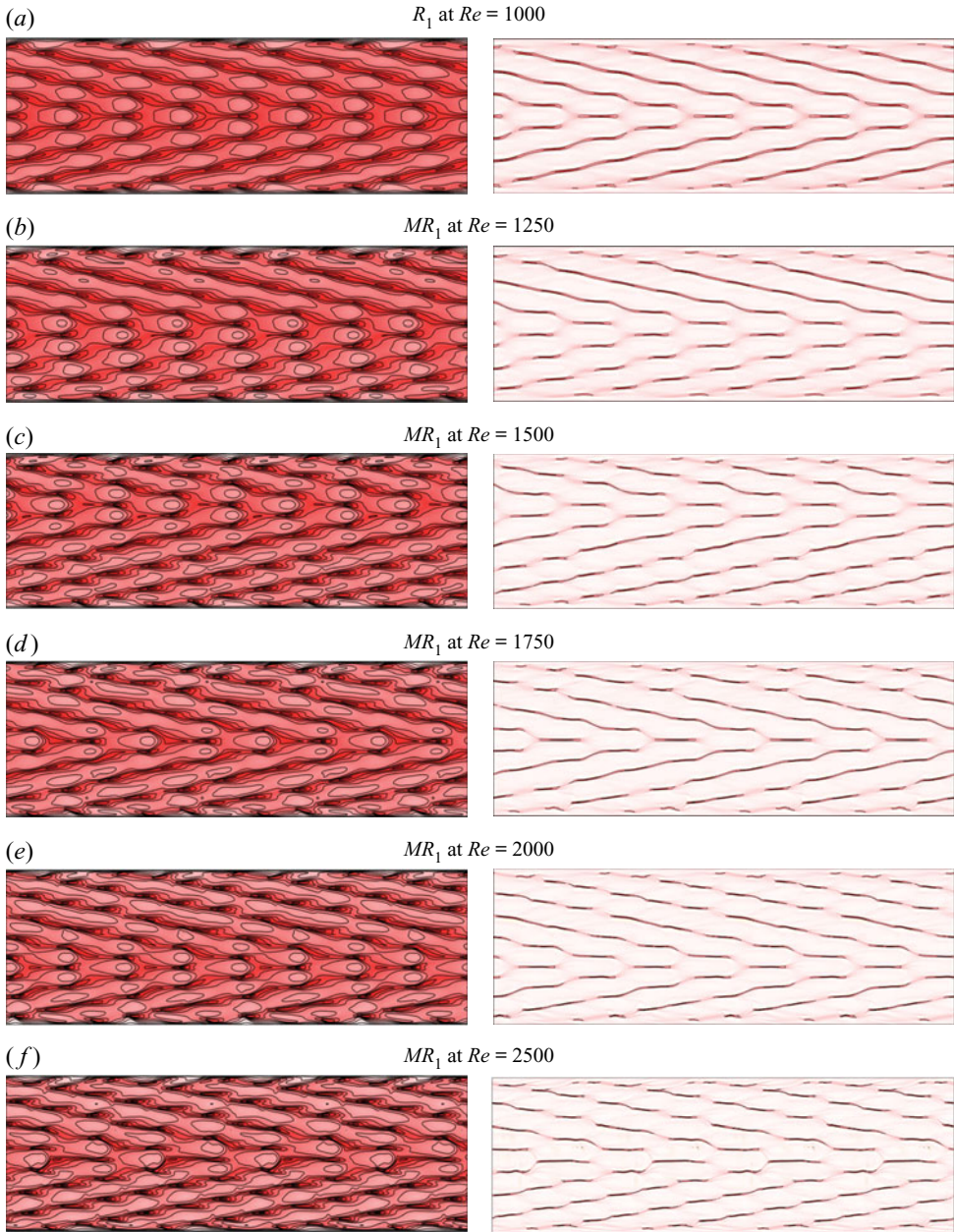


Figure 16. Space-time contour plots (t, z) of Γ (left) and $\partial_z T$ (right) at $\theta = 0$ and $r = r_i + 0.1$ over four precession periods for R_1 and MR_1 at Re as indicated. Three (eight) contour levels between 0 and the maximum value for $\partial_z T$ (Γ).

\mathcal{K} symmetry, although the frequencies lock near the bifurcation point resulting in single frequency periodic flow. In the present problem, with larger $\eta = 0.417$, the spiral waves are not present, and the instability takes the form of what may loosely be described as flat Taylor vortices with small axial wavelength that are not axisymmetric; they are broken in half azimuthally and the halves are axially displaced approximately half a wavelength

Stratified Taylor–Couette flow: nonlinear dynamics

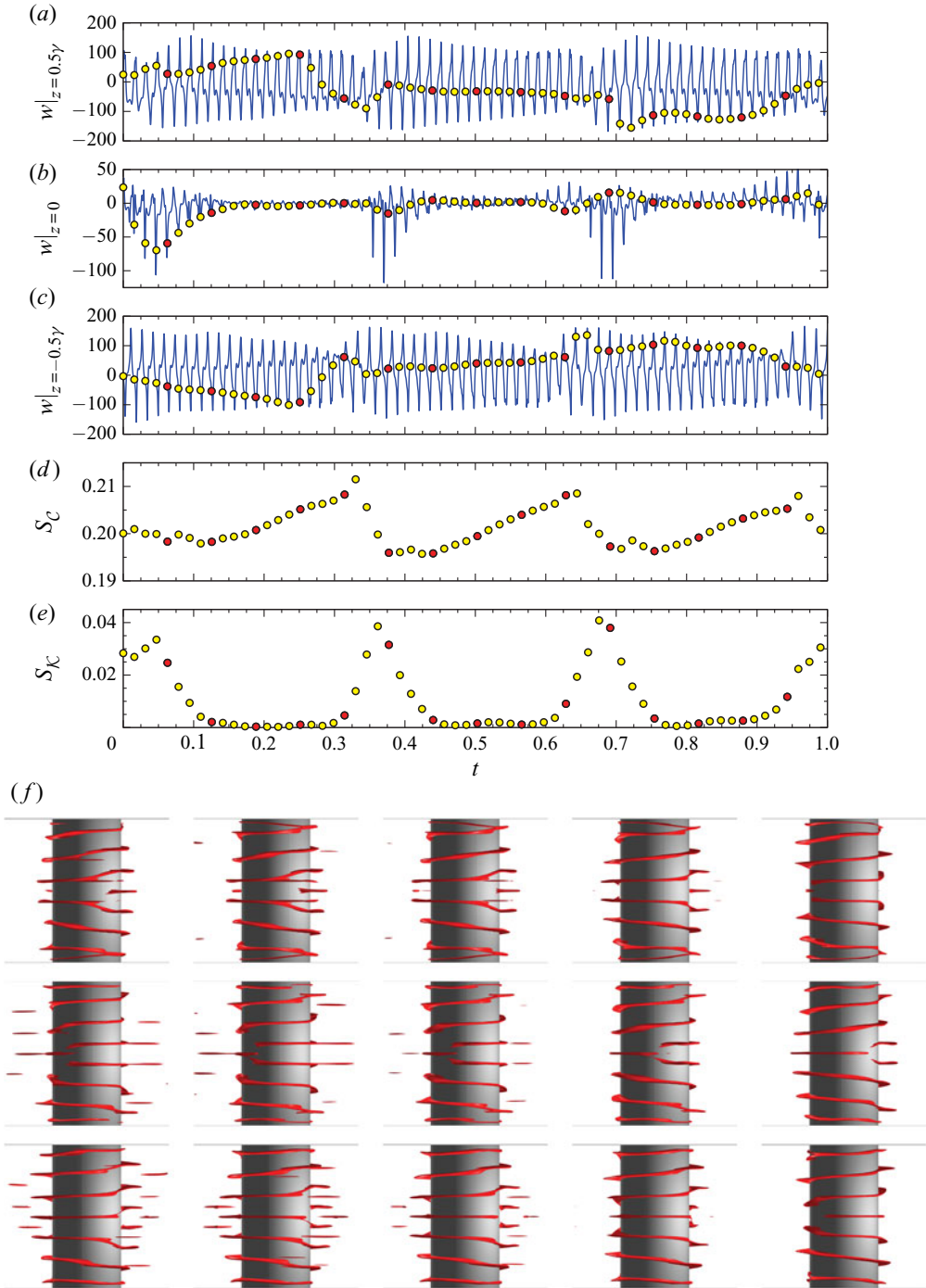


Figure 17. The modulated rotating wave MR_1 at $Re = 1250$: (a–c) time series of the axial velocity w at $(r, \theta) = (r_i + 0.05, 0)$ and z as indicated, over one viscous time covering three periods of ω_2 ; (d, e) time series of the symmetry measures S_C and $S_{\mathcal{C}}$. The yellow symbols are strobed at the precession frequency ω_p , and correspond to the frames in movie 3. (f) Frames selected from movie 3, showing isosurfaces of $\partial_z T$ at times indicated by red symbols in (a) to (e).

(this is reminiscent of the experimental observations by Boubnov *et al.* (1996)). So, like the helical waves in the small η flows, they have azimuthal wavenumber $m = 1$, but they are not smooth helical waves.

In both the small η study (Lopez & Marques 2020) and the present medium η study, the ratio of rotation to buoyancy frequency was $Fr = 0.53$. However, in the much smaller η case the helical waves from the instability remain localized to the rotating inner cylinder, and their onset is at $Re \sim 6 \times 10^3$. This critical Re is twenty times larger than for the medium $\eta = 0.417$ studied here. As a consequence, the effects of centrifugal buoyancy near onset are much weaker in the present study. In the small η experiments (Flór *et al.* 2018) and numerical simulations (Lopez & Marques 2020), centrifugal buoyancy leads to the lower corner losing stability at a lower Re than the top corner, and these localized perturbations have slightly different frequencies. However, in the present medium η study, it appears that due to viscous effects together with the small value of $\epsilon \sim 10^{-4}$ (quantifying the strength of the centrifugal buoyancy), the two instability wave frequencies lock and the whole flow is a single frequency periodic flow (a rotating wave) over a wide range of Re , from onset at $Re \approx 340$ up to $Re = 1000$. In laboratory experiments, which often use salt stratification in an annulus with a no-slip bottom and an open top, the up–down \mathcal{K} symmetry is further broken. The details of how the symmetry is broken lead to a very complicated dynamics in a very small neighbourhood of the onset of instability, but further beyond onset the symmetry-broken dynamics becomes less dependent on the details (Pacheco, Lopez & Marques 2011; Marques *et al.* 2013).

Perhaps more important than accounting for centrifugal buoyancy effects is to account for the presence of endwalls in the short aspect ratio, $\gamma = 3$, flows. Endwalls are ignored when studying the linear stability so that a basic unidirectional basic state can be considered; we have shown how different the basic state is in the short finite length annulus. When considering the nonlinear dynamics ignoring endwalls, nonlinear flows are assumed to be axially periodic (with the axial period often being assigned to be the wavelength of the most unstable mode or some integer multiple of that wavelength). The axially periodic system has $SO(2) \times O(2)$ symmetry, where $SO(2)$ corresponds to invariance to rotations about the axis and $O(2) = SO(2) \times Z_2$ corresponds to arbitrary axial translations, $SO(2)$, and reflections about any axial level, Z_2 . In the finite annulus, ignoring centrifugal buoyancy, the system has $SO(2) \times Z_2$ symmetry, with Z_2 being the mid-height reflection. With the idealized $O(2)$ symmetry, the primary non-axisymmetric instability in stratified Taylor–Couette flows is to spiral waves of opposite chirality, called ribbons, or if the axial symmetry is broken then mixed-ribbons or cross-spirals result (Leclercq *et al.* 2016*b*). Without endwalls, these nonlinear states can have a non-zero net axial mass flux. The presence of endwalls (or even if the top surface is open) enforces a zero net axial mass flux. For very large aspect ratios, this can be enforced numerically by allowing a finite axial pressure gradient which recovers the correct global recirculation in the capped annulus (Marques & Lopez 1997), but for short aspect ratio annuli, it is easier and more correct to directly model the endwalls, as is done in the present study. Furthermore, stratified flow in an axially infinite annulus is conceptually problematic, particularly within the Boussinesq approximation.

One of the more spectacular features of the stratified Taylor–Couette flows studied here is the formation of layers immediately following the onset of instability. These layers – regions of uniform density separated by much thinner regions of large axial density gradient – are observed in many stratified shear flows, but there is no general consensus on how they come about nor on how their length scales are set (see Thorpe (2016), for a discussion of various candidate mechanisms). There continues to be great interest in addressing these open questions (Caulfield 2020, 2021), as is reflected in a

recent research program (Diamond *et al.* 2021), where the $\eta = 0.417$, $\gamma = 3$ stratified Taylor–Couette flow was held up as an example laboratory experiment in which this layering is observed. There remain open questions, such as whether linear instability sets the layering scales. The results of our simulations of this flow at least establish that the primary instability – resulting from the competition between a Rayleigh unstable angular momentum distribution, stable stratification inhibiting axial variations and viscous damping – does account for the spatio-temporal layered structures. The large density gradients occur precisely where the strong radial jets of angular momentum leaving the inner cylinder boundary layer form. Near onset, the axial spacing between these jets is $\lambda \approx 0.6$, corresponding to five jets in the $\eta = 0.417$, $\gamma = 3$ annulus, and the number of jets increase with Re . The jets are not axisymmetric, they have azimuthal wavenumber $m = 1$ but are not smooth in azimuth. They precess in azimuth at approximately one third the rotation rate of the inner cylinder, with this precession rate a slowly decreasing function of Re .

Supplementary movies. Supplementary movies are available at <https://doi.org/10.1017/jfm.2021.893>.

Funding. This work was supported by the Spanish Ministry of Education and Science/FEDER grants FIS2017-85794-P and PRX18/00179.

Declaration of interests. The authors report no conflict of interest.

Author ORCIDs.

 Juan M. Lopez <https://orcid.org/0000-0002-4580-6505>;

 Francisco Marques <https://orcid.org/0000-0003-4921-9495>.

REFERENCES

- ABSHAGEN, J., LOPEZ, J.M., MARQUES, F. & PFISTER, G. 2005*a* Mode competition of rotating waves in reflection-symmetric Taylor–Couette flow. *J. Fluid Mech.* **540**, 269–299.
- ABSHAGEN, J., LOPEZ, J.M., MARQUES, F. & PFISTER, G. 2005*b* Symmetry breaking via global bifurcations of modulated rotating waves in hydrodynamics. *Phys. Rev. Lett.* **94**, 074501.
- ABSHAGEN, J., LOPEZ, J.M., MARQUES, F. & PFISTER, G. 2008 Bursting dynamics due to a homoclinic cascade in Taylor–Couette flow. *J. Fluid Mech.* **613**, 357–384.
- ANDERECK, C.D., LIU, S.S. & SWINNEY, H.L. 1986 Flow regimes in a circular Couette system with independently rotating cylinders. *J. Fluid Mech.* **164**, 155–183.
- AVILA, M. 2012 Stability and angular-momentum transport of fluid flows between corotating cylinders. *Phys. Rev. Lett.* **108**, 124501.
- AVILA, M., GRIMES, M., LOPEZ, J.M. & MARQUES, F. 2008 Global endwall effects on centrifugally stable flows. *Phys. Fluids* **20**, 104104.
- BENJAMIN, T.B. & MULLIN, T. 1981 Anomalous modes in the Taylor experiment. *Proc. R. Soc. Lond. A* **377**, 221–249.
- BOUBNOV, B.M., GLEDZER, E.B. & HOPFINGER, E.J. 1995 Stratified circular Couette flow: instability and flow regimes. *J. Fluid Mech.* **292**, 333–358.
- BOUBNOV, B.M., GLEDZER, E.B., HOPFINGER, E.J. & ORLANDI, P. 1996 Layer formation and transitions in stratified circular Couette flow. *Dyn. Atmos. Oceans* **23**, 139–153.
- BURIN, M.J., JI, H., SCHARTMAN, E., CUTLER, R., HEITZENROEDER, P., LIU, W., MORRIS, L. & RAFTOPOULOS, S. 2006 Reduction of Ekman circulation within Taylor–Couette flow. *Exp. Fluids* **40**, 962–966.
- CATON, F., JANIAUD, B. & HOPFINGER, E.J. 1999 Primary and secondary Hopf bifurcations in stratified Taylor–Couette flow. *Phys. Rev. Lett.* **82**, 4647–4650.
- CATON, F., JANIAUD, B. & HOPFINGER, E.J. 2000 Stability and bifurcations in stratified Taylor–Couette flow. *J. Fluid Mech.* **419**, 93–124.
- CAULFIELD, C.P. 2020 Open questions in turbulent stratified mixing: do we even know what we do not know? *Phys. Rev. Fluids* **5**, 110518.
- CAULFIELD, C.P. 2021 Layering, instabilities, and mixing in turbulent stratified flows. *Annu. Rev. Fluid Mech.* **53**, 113–145.

- CLIFFE, K.A., KOBINE, J.J. & MULLIN, T. 1992 The role of anomalous modes in Taylor–Couette flow. *Proc. R. Soc. Lond. A* **439**, 341–357.
- COLES, D. 1965 Transition in circular Couette flow. *J. Fluid Mech.* **21**, 385–425.
- COLES, D. & VAN ATTA, C. 1966 Measured distortion of a laminar circular Couette flow by end effects. *J. Fluid Mech.* **25**, 513–521.
- DIAMOND, P.H., GARAUD, P., HUGHES, D.W. & SUTHERLAND, B. (Eds) 2021 *KITP Program: Layering in Atmospheres, Oceans and Plasmas*. University of California Santa Barbara.
- FLÓR, J.B., HIRSCHBERG, L., OOSTENRIJK, B.H. & VAN HEIJST, G.J.F. 2018 Onset of centrifugal instability at a rotating cylinder in a stratified fluid. *Phys. Fluids* **30**, 084103.
- GELLERT, M. & RÜDIGER, G. 2009 Stratorotational instability in Taylor–Couette flow heated from above. *J. Fluid Mech.* **623**, 375–385.
- GRAYRER, H., YALIM, J., WELFERT, B.D. & LOPEZ, J.M. 2020 Dynamics in a stably stratified tilted square cavity. *J. Fluid Mech.* **883**, A62.
- GROSSMANN, S., LOHSE, D. & SUN, C. 2015 High-Reynolds number Taylor–Couette turbulence. *Annu. Rev. Fluid Mech.* **48**, 53–80.
- HUA, B.L., LE GENTIL, S. & ORLANDI, P. 1997a First transitions in circular Couette flow with axial stratification. *Phys. Fluids* **9**, 365–375.
- HUA, B.L., MOORE, D.W. & LE GENTIL, S. 1997b Inertial nonlinear equilibration of equatorial flows. *J. Fluid Mech.* **331**, 345–371.
- IBANEZ, R., SWINNEY, H.L. & RODENBORN, B. 2016 Observations of the stratorotational instability in rotating concentric cylinders. *Phys. Rev. Fluids* **1**, 053601.
- LE BARS, M. & LE GAL, P. 2007 Experimental analysis of the stratorotational instability in a cylindrical Couette flow. *Phys. Rev. Lett.* **99**, 064502.
- LECLERCQ, C., NGUYEN, F. & KERSWELL, R.R. 2016a Connections between centrifugal, stratorotational, and radiative instabilities in viscous Taylor–Couette flow. *Phys. Rev. E* **94**, 043103.
- LECLERCQ, C., PARTRIDGE, J.L., AUGIER, P., CAULFIELD, C.P., DALZIEL, S.B. & LINDEN, P.F. 2016b Nonlinear waves in stratified Taylor–Couette flow. Part 1. Layer formation. [arXiv:1609.02885](https://arxiv.org/abs/1609.02885).
- LECLERCQ, C., PARTRIDGE, J.L., AUGIER, P., DALZIEL, S.B. & KERSWELL, R.R. 2016c Using stratification to mitigate end effects in quasi-Keplerian Taylor–Couette flow. *J. Fluid Mech.* **791**, 608–630.
- LECLERCQ, C., PARTRIDGE, J.L., CAULFIELD, C.P., DALZIEL, S.B. & LINDEN, P.F. 2016d Nonlinear waves in stratified Taylor–Couette flow. Part 2. Buoyancy flux. [arXiv:1609.02886](https://arxiv.org/abs/1609.02886).
- LOPEZ, J.M. 1998 Characteristics of endwall and sidewall boundary layers in a rotating cylinder with a differentially rotating endwall. *J. Fluid Mech.* **359**, 49–79.
- LOPEZ, J.M. 2016 Subcritical instability of finite circular Couette flow with stationary inner cylinder. *J. Fluid Mech.* **793**, 589–611.
- LOPEZ, J.M. & MARQUES, F. 2003 Small aspect ratio Taylor–Couette flow: onset of a very-low-frequency three-torus state. *Phys. Rev. E* **68**, 036302.
- LOPEZ, J.M. & MARQUES, F. 2005 Finite aspect ratio Taylor–Couette flow: Shil’nikov dynamics of 2-tori. *Physica D* **211**, 168–191.
- LOPEZ, J.M. & MARQUES, F. 2014 Three-dimensional instabilities in a discretely heated annular flow: onset of spatio-temporal complexity via defect dynamics. *Phys. Fluids* **26**, 064102.
- LOPEZ, J.M. & MARQUES, F. 2020 Impact of centrifugal buoyancy on strato-rotational instability. *J. Fluid Mech.* **890**, A9.
- LOPEZ, J.M., MARQUES, F. & AVILA, M. 2013 The boussinesq approximation in rapidly rotating flows. *J. Fluid Mech.* **737**, 56–77.
- LOPEZ, J.M., MARQUES, F. & SHEN, J. 2004 Complex dynamics in a short annular container with rotating bottom and inner cylinder. *J. Fluid Mech.* **51**, 327–354.
- MARQUES, F. & LOPEZ, J.M. 1997 Taylor–Couette flow with axial oscillations of the inner cylinder: Floquet analysis of the basic flow. *J. Fluid Mech.* **348**, 153–175.
- MARQUES, F. & LOPEZ, J.M. 2006 Onset of three-dimensional unsteady states in small aspect-ratio Taylor–Couette flow. *J. Fluid Mech.* **561**, 255–277.
- MARQUES, F. & LOPEZ, J.M. 2015 Precession of a rapidly rotating cylinder flow: traverse through resonance. *J. Fluid Mech.* **782**, 63–98.
- MARQUES, F., MESEGUER, A., LOPEZ, J.M., PACHECO, J.R. & LOPEZ, J.M. 2013 Bifurcations with imperfect $SO(2)$ symmetry and pinning of rotating waves. *Proc. R. Soc. Lond. A* **469**, 20120348.
- MELETTI, G., ABIDE, S., VIAZZO, S., KREBS, A. & HARLANDER, U. 2021 Experiments and long-term high-performance computations on amplitude modulations of strato-rotational flows. *Geophys. Astrophys. Fluid Dyn.* **115**, 297–321.

Stratified Taylor–Couette flow: nonlinear dynamics

- MOLEMAKER, M.J., MCWILLIAMS, J.C. & YAVNEH, I. 2001 Instability and equilibration of centrifugally stable stratified Taylor–Couette flow. *Phys. Rev. Lett.* **86**, 5270–5273.
- OGLETHORPE, R.L.F., CAULFIELD, C.P. & WOODS, A.W. 2013 Spontaneous layering in stratified turbulent Taylor–Couette flow. *J. Fluid Mech.* **721**, R3.
- PACHECO, J.R., LOPEZ, J.M. & MARQUES, F. 2011 Pinning of rotating waves to defects in finite Taylor–Couette flow. *J. Fluid Mech.* **666**, 254–272.
- PARK, J. & BILLANT, P. 2013 The stably stratified Taylor–Couette flow is always unstable except for solid-body rotation. *J. Fluid Mech.* **725**, 262–280.
- PARTRIDGE, J.L., LECLERCQ, C., CAULFIELD, C.P. & DALZIEL, S.B. 2016 Layer formation in stratified Taylor–Couette flow. In *VIIIth International Symposium on Stratified Flows, San Diego, USA*.
- ROBINS, L.J.M., KERSALÉ, E. & JONES, C.A. 2020 Viscous and inviscid strato-rotational instability. *J. Fluid Mech.* **894**, A13.
- RÜDIGER, G., SEELIG, T., SCHULTZ, M., GELLERT, M., EGBERS, C. & HARLANDER, U. 2017 The stratorotational instability of Taylor–Couette flows with moderate Reynolds numbers. *Geophys. Astrophys. Fluid Dyn.* **111**, 429–447.
- SHALYBKOV, D. & RÜDIGER, G. 2005 Stability of density-stratified viscous Taylor–Couette flows. *Astron. Astrophys.* **438**, 411–417.
- TAGG, R.P. 1994 The Couette–Taylor problem. *Nonlinear Sci. Today* **4**, 1–25.
- TAYLOR, G.I. 1923 Stability of a viscous liquid contained between two rotating cylinders. *Phil. Trans. R. Soc. A* **223**, 289–343.
- THORPE, S.A. 1966 The stability of stratified Couette flow. In *Notes on the 1966 Summer Study Program in Geophysical Fluid Dynamics*, pp. 80–107. Woods Hole Oceanographic Inst.
- THORPE, S.A. 2016 Layers and internal waves in uniformly stratified fluids stirred by vertical grids. *J. Fluid Mech.* **793**, 380–413.
- WATANABE, T., FURUKAWA, H. & NAKAMURA, I. 2002 Nonlinear development of flow patterns in an annulus with decelerating inner cylinder. *Phys. Fluids* **14**, 333–341.
- WITHJACK, E.M. & CHEN, C.F. 1974 An experimental study of Couette instability of stratified fluids. *J. Fluid Mech.* **66**, 725–737.
- WITHJACK, E.M. & CHEN, C.F. 1975 Stability analysis of rotational Couette flow of stratified fluids. *J. Fluid Mech.* **68**, 157–175.
- WOODS, A.W., CAULFIELD, C.P., LANDEL, J.R. & KUESTERS, A. 2010 Non-invasive turbulent mixing across a density interface in a turbulent Taylor–Couette flow. *J. Fluid Mech.* **663**, 347–357.
- YALIM, J., WELFERT, B.D. & LOPEZ, J.M. 2019 Parametrically forced stably stratified cavity flow: complicated nonlinear dynamics near the onset of instability. *J. Fluid Mech.* **871**, 1067–1096.
- YAVNEH, I., MCWILLIAMS, J.C. & MOLEMAKER, M.J. 2001 Non-axisymmetric instability of centrifugally stable stratified Taylor–Couette flow. *J. Fluid Mech.* **448**, 1–21.